An NIR-propelled janus nanomotor with enhanced ROS-scavenging, immunomodulating and biofilm-eradicating capacity for periodontitis treatment

Xuan Bai [1], Wenan Peng [1], Ying Tang, Ziming Wang, Jingmei Guo, Fangfang Song, Hongye Yang, Cui Huang [*]

State Key Laboratory of Oral & Maxillofacial Reconstruction and Regeneration, Key Laboratory of Oral Biomedicine Ministry of Education, Hubei Key Laboratory of Stomatology, School & Hospital of Stomatology, Wuhan University, Wuhan, 430079, China

ARTICLE INFO

ABSTRACT

Periodontitis is an inflammatory disease caused by bacterial biofilms, which leads to the destruction of periodontal tissue. Current treatments, such as mechanical cleaning and antibiotics, struggle to effectively address the persistent biofilms, inflammation, and tissue damage. A new approach involves developing a Janus nanomotor (J-CeM@Au) by coating cerium dioxide-doped mesoporous silica (CeM) with gold nanoparticles (AuNPs). This nanomotor exhibits thermophoretic motion when exposed to near-infrared (NIR) laser light due to the temperature gradient produced by the photothermal effects of asymmetrically distributed AuNPs. The NIR laser provides the energy for propulsion and activates the nanomotor's antibacterial properties, allowing it to penetrate biofilms and kill bacteria. Additionally, the nanomotor's ability to scavenge reactive oxygen species (ROS) can modulate the immune response and create a regenerative environment, promoting the healing of periodontal tissue. Overall, this multifunctional nanomotor offers a promising new approach for treating periodontitis by simultaneously addressing biofilm management and immune modulation with autonomous movement.

1. Introduction

Periodontitis is a chronic inflammatory disease that characterized by the progressive destruction of the periodontium, which can ultimately lead to tooth loss. Periodontitis, ranked as the sixth most prevalent chronic disease worldwide, has emerged as a significant public health issue in the field of oral health [1]. Extensive evidence supports the strong correlation between periodontitis and systemic conditions such as cardiovascular disease and diabetes mellitus [2]. The pathogenesis of periodontitis is intricate. It is initiated by bacterial biofilms and exacerbated by the disruption of the delicate balance between bacterial virulence and host immunity [3,4]. The transition from a healthy periodontium to an inflammatory state involves a shift in the microbial community from symbiotic to dysbiosis, with pathogenic bacteria playing a pivotal role. Keystone pathogens such as *Porphyromonas gingivalis* (*P. g*) and *Fusobacterium nucleatum* (*F. n*) promote the progression of periodontitis by evading host defense and causing tissue damage

through their virulence factors [5]. For example, lipopolysaccharides (LPS) from *P. g* are recognized by Toll-like receptors (TLRs), impairing macrophages' phagocytic and bactericidal capabilities via TLR2-PI3K signaling pathway [6]. In addition, tolerance induced by *P. g* LPS alters immune responses in neutrophils, diminishing their ability to resist bacterial invasion [7]. *F. n* is a well-known bridging species that mediates the coaggregation of aerobic and strictly anaerobic bacteria, which is crucial for biofilm maturation [8].

Unfortunately, the maladjusted pathogenic microorganisms will cause dysregulation of the host immune responses mediated by immune cells through immunoglobulins, complement proteins, and cytokine production, which is the main factor to aggravate periodontal tissue destruction. Among immune cells, macrophages play a crucial role in the human innate immune system as they identify and phagocytose bacteria, and produce cytokines to mediate immune-inflammatory responses [9]. Macrophages can be broadly classified into two phenotypes: classical activated macrophages (M1 phenotype) and alternatively activated

macrophages (M2 phenotype) [10]. M1 macrophages are closely associated with the progression of periodontitis as they release pro-inflammatory cytokines, such as TNF-α and IL-6, promoting periodontal infection and alveolar bone resorption [11]. M2 macrophages are associated with the remission of periodontitis as they secrete anti-inflammatory cytokines such as IL-4 and IL-10, facilitating periodontal tissue healing and bone remodeling [12]. Therefore, it is imperative to manipulate macrophage polarization, particularly increasing the abundance of M2-type macrophages for the treatment of periodontitis.

Currently, the primary treatment strategies for periodontitis involve mechanical debridement, antibiotic application, and surgical procedures [13,14]. Nevertheless, the deep-seated biofilms are hard to eliminate because of the complex anatomy of teeth, such as root furcation, enamel pearl et al. [15]. These areas are difficult to reach, and biofilms firmly adhere to the root surface, further compromising the therapeutic efficacy of anti-biofilm agents and causing a persistent inflammatory response. Meanwhile, antibiotic resistance has become significant concern in modern treatment for periodontitis [16]. To address this issue, researchers have been exploring materials with selective antimicrobial properties in recent years [17]. However, there is still room for improvement in both the antimicrobial efficacy and immunomodulatory capabilities of these antimicrobial materials specifically targeting certain pathogens. All in all, it is imperative to discover new approaches to overcome the constraints of conventional therapeutic techniques.

With increasing evidences on the important role of reactive oxygen species (ROS) in the progression of periodontitis, the utilization of ROS-scavenging strategies holds promise in modulating the inflammatory microenvironment caused by bacterial infection. During chronic inflammation, LPS of pathogens induces the generation of ROS [18]. Consequently, the excessive ROS can inflict significant damage on normal tissues through lipid peroxidation, protein denaturation, and DNA damage, thereby impeding the self-healing process of periodontal tissues [19]. Moreover, as signaling molecules, excessive ROS can exacerbate the inflammatory cascade in periodontitis by inducing the production of pro-inflammatory cytokines including interleukin-1β (IL-1β) and tumor necrosis factor-α (TNF-α), and chemokines such as chemokine (C–C motif) ligand 2 (CCL2) and chemokine (C-X-C motif) ligand 8 (CXCL8) [20]. These cytokines and chemokines directly inhibit the osteogenic potential of stem cells and enhance osteoclast activity, leading to significant bone resorption [21]. In addition, as a crucial cellular mediator, ROS can activate pro-inflammatory signaling pathways like nuclear factor-kappa B (NF-κB) pathway to induce M1 macrophage polarization during the onset and progression of periodontitis [22]. This process ultimately results in gingival fibroblast apoptosis and alveolar bone resorption [23]. Hence, the rational modulation of ROS level in the local microenvironment in periodontitis is a promising way to alleviate oxidative stress injury, ameliorate bacterial-mediated immune dysregulation and facilitate osteogenesis for periodontal healing. In this context, a growing number of studies have demonstrated that the application of antioxidants can promote the alleviation of inflammation in periodontitis. For example, Guo and colleagues fabricated Ru-porphyrin-networks (Ru-Por-Net)-based reactive oxygen nanobiocatalysts (ROBCs), which effectively alleviated local tissue inflammation and bone resorption in periodontitis by catalytic elimination of ROS [24]. Xie and co-workers developed an artificial antioxidase called CoO–Ir, which significantly mitigated inflammatory responses in periodontitis by cascade ·O_2^- and H_2O_2 scavenging [25].

Among various antioxidants, cerium dioxide (CeO_2) nanoenzyme has garnered significant attention from numerous scholars due to its superoxide dismutase (SOD)-mimetic and catalase (CAT)-mimetic activities [26,27]. It possesses automatic regeneration of redox cycling ability, facilitated by the valence state transformation between Ce^{3+} and Ce^{4+} [28]. Moreover, it exhibits chemical stability and excellent biocompatibility for biomedical applications, for example, Pezzini et al. discovered that CeO_2 displayed antioxidant effects at the cellular level

and directly impacted mitochondrial functions, serving as a pro-energetic agent [29]. Although CeO_2 exhibits favorable enzyme-mimetic activity, its antioxidant capacity is less efficient compared to natural antioxidant enzymes [30]. Researchers have explored various approaches, such as morphological control and surface modification, to enhance the catalytic performance of CeO_2 [31]. Nevertheless, the current effectiveness of CeO_2 in scavenging ROS is unsatisfactory due to its insufficient antioxidant activity [32]. Hence, it remains crucial challenges in the design of antioxidant nanoagents to enhance ROS-scavenging efficiency and reduce underlying biotoxicity in high-dose usage.

Therefore, current treatments for periodontitis often require a combination of antimicrobial and anti-inflammatory therapies with excellent biocompatibility to restore local periodontal immune homeostasis. Considering the adverse effects of antibiotic application, photothermal therapy (PTT) is a promising way for combating bacteria and biofilms by virtue of its lack of drug resistance, controllability, and noninvasiveness [33]. In theory, PTT inflicts fatal damage on bacteria through the use of photothermal agents (PTAs), which convert light energy into thermal energy under the irradiation of an external light source such as near-infrared (NIR) laser, leading to protein denaturation and membrane disruption [34]. As a core part of PTT, PTAs has been intensively studied in recent years. A variety of new materials have emerged, which can be broadly categorized as inorganic PTAs and organic PTAs. Among these PTAs, gold nanoparticles (AuNPs), with excellent biocompatibility, photothermal property, and light stability, have been widely used by scientists in PTT [35,36]. Notably, AuNPs can significantly absorb NIR light at 808 nm and show high photothermal conversion efficiency under 808 nm NIR light [37]. Biomaterials based on AuNPs with 808 nm NIR light exhibit significant potential in biomedical applications, including anti-tumor treatment and antibacterial therapy [38]. However, conventional PTAs exhibit limited-efficiency as they are immobile and only function *in situ* [39]. Consequently, the common approach to enhance the therapeutic impact is to administer therapeutic agents at a higher dosage [40], which is prone to cause undesirable complications including renal toxicity, inflammatory reactions and necrosis of tissues et al. [41]. Therefore, it is essential to explore new methods to improve the efficiency of PTT.

With the rapid development of molecular nanotechnology, the nanomotors are able to transform various types of external power (chemical, ultrasound, optical energy) into kinetic motion, making them highly promising for biomedical applications such as drug delivery, biosensing, and overcoming biological barriers [42]. By combining nanomotors with PTAs and antioxidant agents, they could potentially yield more potent antibacterial and anti-inflammatory effect. For example, Maric et al. developed a SiO_2–Au nanomotor that operated through NIR light irradiation, exhibiting a significant impact on the eradication of *Pseudomonas aeruginosa* biofilm [43]. In addition, Zhang and coworkers produced a movable BPQDs-modified Janus Pt/SiO_2 nanomotors activated by decomposition of H_2O_2, which showed enhanced ROS scavenging efficiency *in vitro* and *in vivo,* thus relieving the ear inflammation in mice [44].

In this study, we developed an asymmetrical Janus nanomotor (J-CeM@Au) that incorporating CeO_2-loaded mesoporous silica as a matrix and partially coated with AuNPs. With the irradiation of NIR laser, J-CeM@Au acts as a nano-sweeper to remove troublesome biofilms and excess ROS. Specifically speaking, firstly, the CeO_2 loaded on the J-CeM@Au is able to scavenge excess ROS of periodontal microenvironment, thereby reducing the inflammatory burden. Secondly, the presence of AuNPs on the J-CeM@Au nanomotor enables the conversion of optical power into thermal energy when exposed to NIR laser, resulting in bactericidal effects. More importantly, the photothermal effect generated by half-coated Au shell also creates a temperature gradient that propels the movement of nanomotor, further facilitating its penetration and clearance of biofilms. Last but not the least, due to the enhanced ROS scavenging efficiency, J-CeM@Au nanomotor
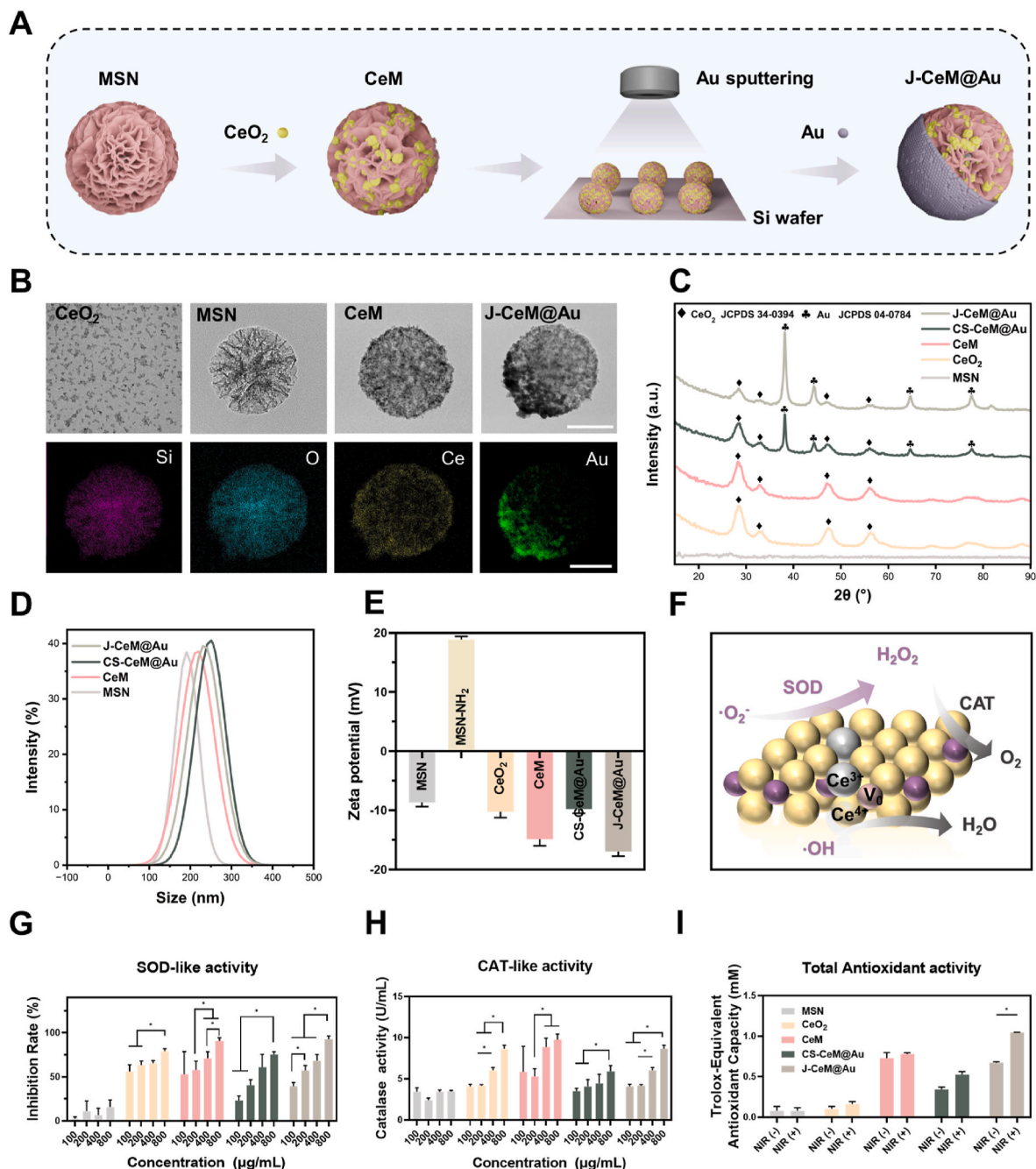
Fig. 1. Characterization and ROS-elimination activities of J-CeM@Au. (A) Schematic illustration of the preparation process of J-CeM@Au. (B) TEM images with EDS mapping of CeO₂, MSN, CeM, J-CeM@Au NPs. Scale bar = 100 nm. (C) XRD pattern of different NPs. (D) Size distribution of different NPs. (E) Zeta potential of different NPs. (F) Schematic diagram of the antioxidant enzyme-mimetic activity of CeO_2 NPs. (G) SOD-like activity and (H) CAT-like activity of NPs at different concentration. (I) Total antioxidant activity of MSN (400 μg/mL), CeO_2 (27 μg/mL), CeM (133 μg/mL), CS-CeM@Au (400 μg/mL), J-CeM@Au (400 μg/mL) with and without 808 nm NIR (1 W/cm²) irradiation.

successfully induces macrophage polarization from the M1 to M2 type by inhibiting the NF-κB pathway, which creates a favorable environment for subsequent periodontal regeneration by promoting osteogenic differentiation of human periodontal ligament stem cells (hPDLSCs). This study introduces a novel strategy for combatting periodontitis by employing a movable nanomotor which integrates PTT for antibacterial property, ROS-scavenging and immunomodulation capacity. Besides its application in periodontitis treatment, we believe that our study can provide a fresh perspective for further development and clinical translation of medical nanoplatform which is promising to guarantee the biocompatibility and less biotoxicity of nanoagents through efficient

ROS scavenging and biofilm clearance facilitated by motile nanomotors.

2. Results and discussion

2.1. Characterization and antioxidized catalytic activity of J-CeM@Au

The synthesis procedure of asymmetry J-CeM@Au is illustrated in Fig. 1A. First of all, dendritic mesoporous silica nanoparticles (MSNs) were synthesized according to previously reported methods [45]. TEM images in Fig. 1B showed uniform structure of MSNs with a diameter of 190 nm and dendritic pore structures. Subsequently, aminated
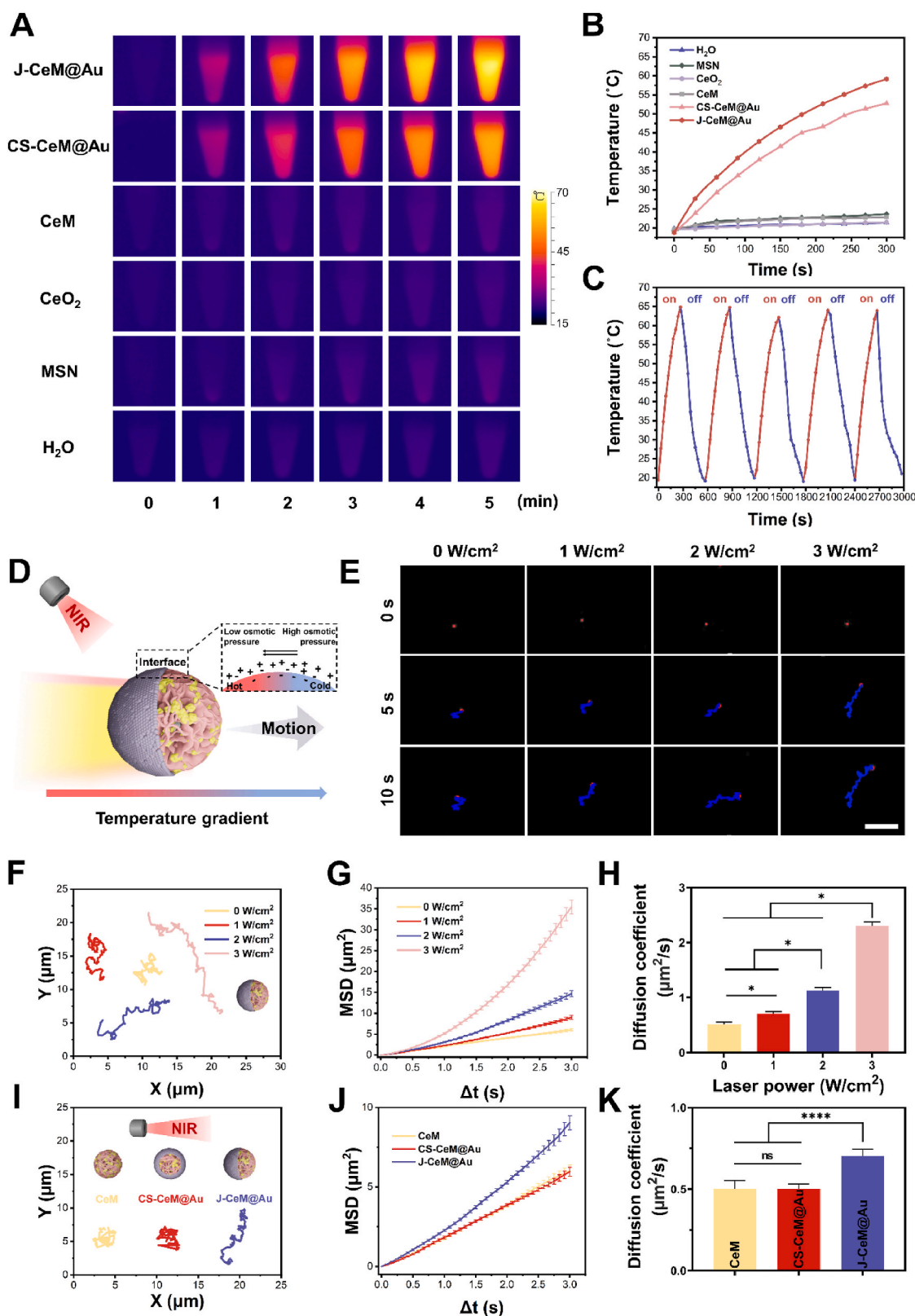
Fig. 2. Photothermal properties and thermophoresis of J-CeM@Au. (A) Infrared thermal photos and (B) temperature-time curve of H_2O, MSN (400 μg/mL), CeO_2 (27 μg/mL), CeM (133 μg/mL), CS-CeM@Au (400 μg/mL) and J-CeM@Au (400 μg/mL). (C) Photostability of J-CeM@Au (400 μg/mL) with 5 heating and cooling cycles under 808 nm NIR (1 W/cm²) irradiation. (D) Schematic illustration of the motion behavior of J-CeM@Au nanomotors. (E)Time-lapse images of J-CeM@Au (red spots) at 0 s, 5 s and 10 s under 808 nm NIR laser irradiation with different powers. Scale bar = 10 μm. (The blue lines represent the paths of J-CeM@Au at different timepoints.) (F) The overall trajectory, (G) MSD and (H) diffusion coefficient of J-CeM@Au under NIR laser irradiation with different powers. (I) The overall trajectory, (J) MSD and (K) diffusion coefficient of CeM, CS-CeM@Au, J-CeM@Au under NIR laser irradiation at 1 W/cm².

mesoporous silica (MSN-NH$_2$) was prepared through amination reaction with APTES. The surface zeta potential of the MSN-NH$_2$ (Fig. 1E) turned to a positive potential value (+18.93 mV) compared with a negative potential value (−8.65 mV) of MSN, indicating the successful amination of silica. Subsequently, quasi-spherical nano ceria with an approximate diameter of 5 nm was synthesized (Fig. 1B). To load CeO$_2$ nanoparticles (CeO$_2$ NPs) onto MSN-NH$_2$, BMPA-capped CeO$_2$ NPs were synthesized and then directly immobilized onto the surface of MSN-NH$_2$ through a combination mechanism involving nucleophilic substitution reaction between bromine and amine group, as well as electrostatic attraction [46]. The resulting MSN-Ceria nanocomposite, denoted as CeM, was observed by TEM. The potential of CeM shifted to a negative value (−14.87 mV) after loading of CeO$_2$ NPs. To prepare Janus NPs, monolayer CeM NPs were spread onto a silicon wafer and the top half of the CeM NPs were coated with AuNPs after electron beam evaporation. The asymmetric structure of J-CeM@Au was observed by TEM with EDS elements mapping, indicating that AuNPs existed on the half surface of J-CeM@Au to form a Janus structure (Fig. 1B). Additionally, to compare the performance differences between Janus nanomotors and common non-Janus NPs, AuNPs were uniformly grown on the CeM to form core-shell structure (CS-CeM@Au) using seed-mediated growth method [47]. The symmetric structure of CS-CeM@Au was observed by TEM with EDS elements mapping (Fig. S1), indicating the uniform distribution of AuNPs on CeM. When coated by AuNPs, both CS-CeM@Au and J-CeM@Au showed a negative potential of −9.75 mV and −16.97 mV, respectively (Fig. 1E). The particle sizes of MSN, CeM, J-CeM@Au and CS-CeM@Au increased in a sequential manner, as shown in Fig. 1D, suggesting the enlargement of nanoparticles (NPs) following different decorations. The NPs exhibited good dispersibility in PBS, as evidenced by Tyndall effects in Fig. S2A. In addition, little changes were observed in the sizes of MSN, CeM, CS-CeM@Au, J-CeM@Au over a week of storage (Fig. S2B-E), indicating the dispersion and stability of these NPs. The XRD patterns in Fig. 1C provided further confirmation of the composition of CeO$_2$ and Au. The XPS survey spectrum in Fig. S3A indicated that J-CeM@Au consisted of silicon, oxygen, cerium, carbon, and aurum elements. Furthermore, the Ce3d spectra results (Fig. S3B) demonstrated the presence of both Ce^{3+} and Ce^{4+} valence states in J-CeM@Au. Consequently, different functional modules including ROS-scavenging, NIR-triggerable movement and photothermal capacities were facilely orchestrated into a Janus nanomotor.

CeO$_2$ NPs exhibit SOD-mimetic and CAT-mimetic activities due to the mixed valence states of Ce^{3+} and Ce^{4+} coexisted on the surface of the Ce oxide lattice [31]. Ce^{4+} can be reduced to Ce^{3+} in the presence of surface oxygen vacancies, therefore effectively reducing ROS levels through the redox reaction [48]. The redox cycling can also be regenerated by automatic valence transformation between Ce^{3+} and Ce^{4+} [48]. Hence, CeO$_2$ and CeO$_2$-containing biomaterials are extensively employed in ROS-scavenging therapy. To evaluate the ROS-scavenging activities of J-CeM@Au, total antioxidant activities were initially examined. As depicted in Fig. S4, the antioxidant activities of CeO$_2$, CeM, CS-CeM@Au, and J-CeM@Au exhibited a dose-dependent trend. Later on, the SOD-like activities (·O$_2^-$ to H$_2$O$_2$) and CAT-like activities (H$_2$O$_2$ to H$_2$O and O$_2$) of NPs were investigated (Fig. 1G and H), which showed a similar dose-dependent trend as total antioxidant activities test. However, MSN exhibited minimal SOD-like and CAT-like activities, suggesting that MSN had no significant impact on ROS-scavenging. The results also revealed that CeM exhibited a higher antioxidant capacity than CeO$_2$ at an equal Ce concentration. Given that the particle size of CeO$_2$ NPs measured approximately 5 nm and aggregation was evident in the TEM image (Fig. 1B), there was a risk of decreased effective surface area [46]. Nevertheless, CeO$_2$ NPs exhibited uniform distribution on the MSN surface (Fig. 1B), effectively mitigating the aggregation of CeO$_2$ NPs. Taken together, we speculated that the enhanced ROS-scavenging ability of CeM could be attributed to the well-dispersed state and increased surface area of CeO$_2$ NPs loaded on MSN, which was in accordance with previous studies [49].

Furthermore, to investigate whether the ROS-scavenging ability of J-CeM@Au could be enhanced by 808 nm NIR irradiation, the total antioxidant activities of NPs without and with NIR irradiation were explored. The results in Fig. 1I showed that the ROS-scavenging ability of J-CeM@Au significantly increased after NIR irradiation compared to the NIR-free control. However, the total antioxidant activities of MSN, CeO$_2$, CeM, and CS-CeM@Au under NIR irradiation remained almost the same as before. Taken together, the above findings demonstrate that J-CeM@Au NPs could efficiently clear multiple types of ROS. Of note, we speculate that the elimination efficiency was significantly enhanced under NIR irradiation by virtue of the active motion induced by thermophoresis, which was similar as previous studies about ROS-scavenging nanomotors [44,50]. In other words, this implies that fewer nanomaterials can achieve improved ROS-scavenging capabilities [50].

2.2. In vitro photothermal and thermophoretic properties of J-CeM@Au

To further validate our hypothesis, the photothermal and thermophoresis performance of J-CeM@Au were studied. As demonstrated in the infrared thermal images (Fig. 2A) and temperature-time curve (Fig. 2B), J-CeM@Au exhibited the most significant temperature increase from 18.78 °C to 59.15 °C. In comparison, CS-CeM@Au, CeM, CeO$_2$, MSN and water reached 52.78 °C, 22.88 °C, 21.48 °C, 23.65 °C and 21.38 °C respectively. Furthermore, J-CeM@Au demonstrated excellent thermal stability even after undergoing five cycles of heating and cooling under 808 nm NIR irradiation (Fig. 2C). Additionally, the photothermal performance of J-CeM@Au can also be controlled by adjusting the concentration and laser intensity, as depicted in Fig. S5A and B.

The results suggested that J-CeM@Au possessed superior photothermal property compared to CS-CeM@Au. According to a previous study by Chen and co-workers, a strong, non-centrosymmetric near-field enhancement (NFE) effect could be realized at the interface between the porphyrin polymersome (PPS) and AuNPs of the asymmetric J-AuPPS NPs. While the NFE effect is not significant in the common non-Janus core-particle Au-PPS nanostructure (CP–AuPPS) [51]. Consequently, the NFE effect results in enhanced light absorption in the NIR region as well as a higher electric/thermal field and a greater concentration of charge carriers at the interfaces of Janus structure [52], which may contribute to the superior photothermal performance of J-CeM@Au compare to CS-CeM@Au.

After confirming the photothermal properties of J-CeM@Au, we proceeded to investigate its thermophoretic behavior. As illustrated in Fig. 2D, NIR light is absorbed by AuNPs on one side of the J-CeM@Au, converting it into thermal energy, while the other side can hardly absorb NIR light, thereby generating a temperature gradient surrounding the Janus nanomotor. The generation of a temperature gradient at the solvent-nanomotor interface leads to the formation of an osmotic pressure gradient parallel to the interface, inducing a thermo-osmotic fluid flow from regions of high to low osmotic pressure along the interface [53]. As the liquid is relatively stationary, this implies that the nanomotor has to move along the temperature gradient opposite to the interfacial fluid flow, which is called thermophoresis [53]. To accurately observe the motion of NPs, CeM, CS-CeM@Au, J-CeM@Au were labeled with Cy3 (orange-red) for visualization under a fluorescence microscope. The videos (Movie S1), time-lapse images (Fig. 2E) and tracked trajectories (Fig. 2F) revealed that J-CeM@Au exhibited random Brownian motion in the absence of NIR laser irradiation. However, as the intensity of the 808 nm NIR laser increased, the distance covered by J-CeM@Au also increased (Fig. 2E and F), indicating enhanced movement of nanomotor. Consistent with the changes in trajectory, the calculated mean square displacement (MSD) curves and the diffusion coefficient of the Janus nanomotors in Fig. 2G and H also increased with the enhancement of laser intensity. Furthermore, the trajectories (Fig. 2I), MSD (Fig. 2J), and diffusion coefficient (Fig. 2K) of CeM,
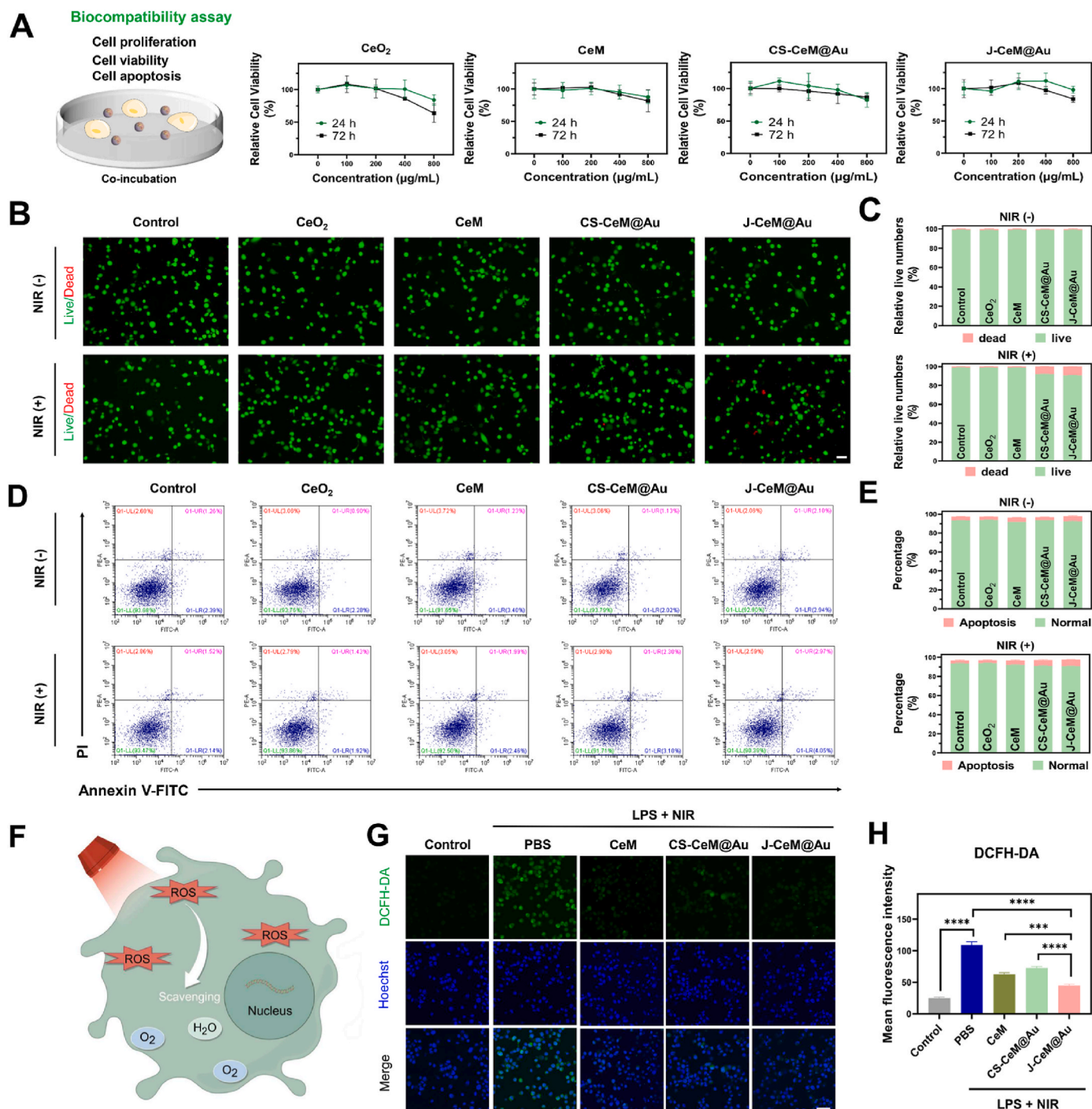
Fig. 3. Cytotoxicity and intracellular ROS level of THP-1-derived macrophage cells cultured in NP suspensions. (A) CCK-8 results of cells cultured in CeO_2, CeM, CS-CeM@Au, J-CeM@Au NP suspensions for 24 h and 72 h. (B) Live/Dead staining images and (C) quantitative analysis of cells cultured in NP suspensions with or without 808 nm NIR laser irradiation. Scale bar = 50 μm. (D) Representative flow cytometry diagram and (E) quantitative analysis of cell apoptosis ratio detected by Annexin V-FITC/PI staining of cells incubated with NP suspensions with or without NIR irradiation. (F) Schematic illustration of intracellular ROS scavenging by J-CeM@Au. (G) Photographs of intracellular ROS level of cells detected by DCFH-DA probe (green) in NP suspensions with 808 nm NIR irradiation and (H) quantitative analysis. Scale bar = 50 μm.

CS-CeM@Au, J-CeM@Au under NIR laser irradiation at 1 W/cm² were analyzed to compare the three different NPs. Evidently, at the same NIR light intensity, the trajectory area of J-CeM@Au exceeded that of CeM and CS-CeM@Au, consistent with the findings in the MSD profiles (Fig. J). In addition, similar outcomes were observed for the diffusion coefficient (Fig. 2K), indicating that the J-CeM@Au nanomotor exhibited the most distinct directional movement among the NPs. Collectively, the J-CeM@Au nanomotor exhibits excellent photothermal and

thermophoresis performance in the presence of 808 nm NIR laser.

2.3. In vitro toxicity assessment and intracellular ROS-scavenging ability of J-CeM@Au

Excellent biocompatibility is a crucial requirement for the application of nanomaterials in disease treatment. CCK-8 results indicated that there was hardly any cytotoxicity to THP-1-derived macrophages when
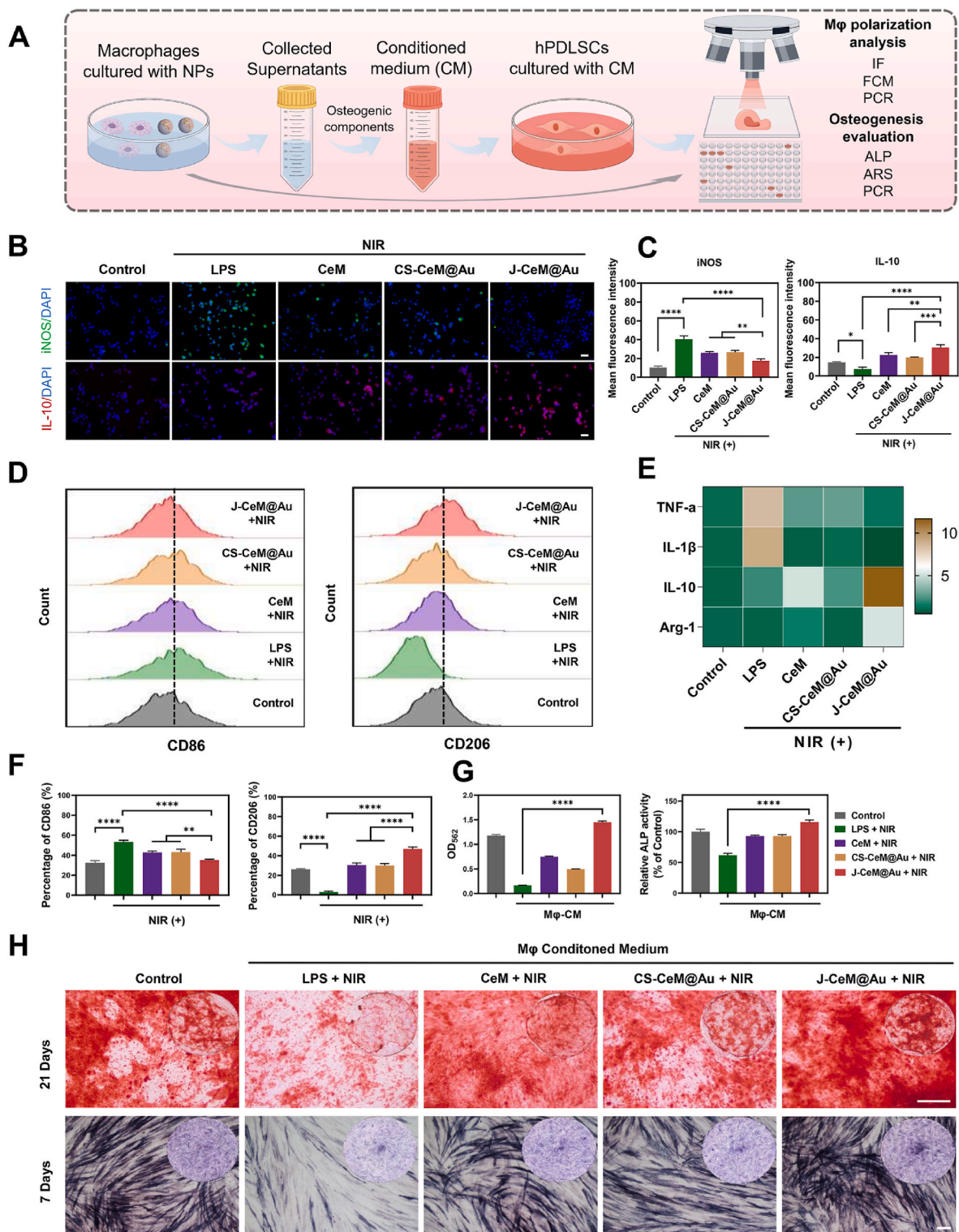
Fig. 4. Macrophages polarization by J-CeM@Au and osteogenic differentiation of hPDLSCs in corresponding Mφ-conditioned medium. (A) Schematic diagram illustrating the experimental procedures of macrophage polarization by different NPs and osteogenic differentiation of hPDLSCs in CM. (B) Immunofluorescence staining photos and (C) fluorescence intensity quantitative analysis of markers (iNOS and IL-10) of THP-1 derived macrophages with different treatments. Scale bar = 50 μm. (D) Representative flow cytometry histograms and (F) quantification analysis of surface markers (CD86 and CD206) of macrophages in different groups. (E) RT-qPCR results of pro-inflammatory and anti-inflammatory mRNA expression of macrophages in different groups. (H) Images and (G) semi-quantification of ARS and ALP staining of hPDLSCs cultured in Mφ-CM of different groups. The scale bars represent 500 μm for the ARS staining (upper row) and 100 μm for the ALP staining (lower row).

the concentration of J-CeM@Au NPs was below 400 μg/mL (Fig. 3A). Considering the concentration of 400 μg/mL exhibited desirable ROS-scavenging ability, J-CeM@Au NPs at this concentration were selected for subsequent experiments. Consequently, CeO₂ (27 μg/mL), CeM (133 μg/mL) and CS-CeM@Au (400 μg/mL), with the same amount of Ce calculated by the ICP result, were chosen as controls. To determine whether J-CeM@Au NPs under NIR irradiation could cause irreversible damages to macrophages, the cell viability was assessed using live/dead staining and apoptosis detection. Calcein acetoxymethyl ester (CAM) and propidium iodide (PI) probes were utilized to stain live cells (green) and dead cells (red), respectively. Fig. 3B, C and Fig. S6A showed that groups without NIR irradiation had few red-stained cells, indicating that the NPs alone at this concentration were nearly harmless to macrophages. Upon NIR irradiation, a small number of red-stained cells were observed in the exothermic CS-CeM@Au and J-CeM@Au groups. Apoptosis detection (Fig. 3D, E and Fig. S6B) indicated that NPs without NIR irradiation did not induce apoptosis in macrophages. While under NIR irradiation, the percentage of apoptotic cells at the early/late stage in J-CeM@Au group exhibited a slight increase to 7.02 %. Nonetheless, the percentage of viable cells remained above 90 %, which was acceptable for subsequent cellular experiments. Collectively, the photothermal effects of J-CeM@Au NPs had negligible harm to macrophages, making them suitable for future biological applications.

Macrophages are the first line of defense in combating pathogens and play crucial roles in the pathological mechanism of periodontitis. Macrophages predominantly express TLR4, making them more responsive to LPS stimulation compared to other non-immune cells like hPDLSCs [54]. In response to pathogens, macrophages secrete pro-inflammatory cytokines that enhance phagocytosis, induce a cascade immune response and eliminate pathogens. Nevertheless, these deleterious cytokines not only contribute to periodontal bone resorption and tissue damage but also hinder the regenerative capacity of stem cells. Accordingly, THP-1 derived macrophages were chosen as target cells for LPS stimulation in our study.

To evaluate the intracellular ROS-scavenging ability of J-CeM@Au in protecting macrophages from oxidative stress injury in the microenvironment of periodontal inflammation, an *in vitro* inflammatory model was established by stimulating macrophages with LPS and the intracellular ROS level was measured using a hypersensitive fluorescent probe called 2′, 7′-dichlorofluorescin diacetate (DCFH-DA). The oxidative stress model is illustrated in Fig. 3F. As is demonstrated in Fig. 3G, H and Fig. S7, a significant increase in intracellular green fluorescence upon LPS stimulation. Notably, NIR irradiation alone or in combination with MSN did not alter the intracellular ROS level. However, CeO₂, CeM, CS-CeM@Au and J-CeM@Au exhibited varying degrees of reduction in intracellular fluorescence intensity, with J-CeM@Au showing the most pronounced effect. The results indicated that CeO₂ effectively eliminated the excessive cellular ROS induced by LPS, and J-CeM@Au exhibited the most significant scavenging rate, potentially due to the active motion of the nanomotor in the inflammatory microenvironment.

2.4. In vitro M2 macrophage polarization and macrophage-induced osteogenic differentiation of hPDLSCs by J-CeM@Au

To further investigate whether the clearance of ROS could alleviate inflammation and promote M2 macrophage polarization. The experimental procedure is depicted in the schematic diagram in Fig. 4A. LPS-primed macrophages were treated with PBS, MSN, CeO₂, CeM, CS-CeM@Au and J-CeM@Au under NIR irradiation. The results of macrophage phenotype identification indicated that LPS-treated macrophages exhibited typical pro-inflammatory M1-like behaviors. As observed in Fig. S8A, after LPS stimulation with or without NIR laser irradiation, the expression of M1-related marker iNOS was enhanced compared to LPS-free control group. Notably, NIR laser alone and MSN were unable to reduce the elevated iNOS level induced by LPS (Fig. 4B, C and Fig. S8A), indicating that they had hardly no effect on the polarized state of

macrophages. However, the polarization state was reversed by NIR-activated J-CeM@Au. As demonstrated in Fig. 4B, upon NIR irradiation, the expression of iNOS exhibited a gradual decrease in CeO₂, CeM, CS-CeM@Au and J-CeM@Au groups, with J-CeM@Au showing the most significant inhibition of M1 macrophage polarization. On the contrary, J-CeM@Au significantly promoted M2 macrophages polarization in all the Ce-containing groups, as evidenced by the increased expression of IL-10 protein observed in the immunofluorescence staining and quantitative analysis (Fig. 4B and C). Representative flow cytometry histograms (Fig. 4D) indicated that J-CeM@Au + NIR reduced the CD86-positive (M1 biomarker) population to the lowest level in all the experimental groups. Conversely, the population of CD206-positive (M2 biomarker) macrophages was maximally increased by J-CeM@Au + NIR across all experimental groups. The quantitative analysis (Fig. 4F) of M1 and M2 macrophages was in accordance with the histogram results. Furthermore, the RT-qPCR results (Fig. 4E) demonstrated that J-CeM@Au + NIR downregulated the expression levels of M1-related genes (IL-1β, TNF-α) and upregulated the expression of M2-related genes (IL-10 and Arg-1) compared to other Ce-containing counterparts. Collectively, these results indicated that J-CeM@Au nanomotor effectively shifted pro-inflammatory M1 macrophages towards anti-inflammatory M2 macrophages, in contrast to CeO₂, CeM, CS-CeM@Au with NIR laser.

Although macrophages are essential in inflammatory-immune response, stem cells such as hPDLSCs, play a vital role in the regeneration of periodontal tissue. Therefore, it is crucial to thoroughly explore the interaction between immune cells and stem cells. As well documented, the anti-inflammatory M2 macrophage can facilitate osteogenic differentiation of hPDLSCs [55,56]. Consequently, we employed macrophage conditioned medium (Mϕ-CM) to induce osteogenic differentiation of hPDLSCs to investigate the role of J-CeM@Au nanomotor in the immune-osteogenic cascade.

Osteogenic differentiation ability was evaluated through alkaline phosphatase (ALP) staining, ALP activity, Alizarin Red S (ARS) staining and detection of osteogenic gene expression. Under LPS-free conditions, the Mϕ-CM slightly enhanced the osteogenic differentiation of hPLDSCs (Fig. S8B), aligning with previous study that M0 macrophages without any stimulation, promoted osteogenesis of BMMSCs [57]. As seen in Fig. 4H, in the LPS-primed medium group, fewer mineralized nodules were seen than that in the control group after incubation for 21 days. However, the J-CeM@Au + NIR medium group exhibited abundant mineralized nodules compared to the CeM and CS-CeM@Au + NIR medium groups, as confirmed by semi-quantitative analysis of ARS staining (Fig. 4G). Results from ALP staining (Fig. 4H) indicated that the LPS-primed medium group exhibited lighter coloration compared to the control group after incubation for 7 days. Nevertheless, the ALP staining in the J-CeM@Au + NIR medium group showed a darker color compared to the CeM and CS-CeM@Au + NIR medium groups. In accordance with the results of ALP stanning, the J-CeM@Au + NIR medium group demonstrated the highest ALP activity among all the Ce-containing medium groups (Fig. 4G). Moreover, mRNA expression levels of the osteogenic gene, including osteopontin (OPN) and ALP, were up-regulated in cells cultured with J-CeM@Au + NIR compared to CeM or CS-CeM@Au + NIR medium groups (Fig. S8C). It's been widely recognized that OPN, an extracellular matrix protein in osseous tissue, plays an important role in the late stage of bone formation by regulating bone mass as well as the quality of mineralization [58]. Therefore, the increased expression of OPN indicated the osteogenic potential of hPDLSCs. The above results demonstrated that Mϕ-CM modulated by LPS apparently weakened the osteogenic differentiation capacity of hPDLSCs. This was primarily because the inflammatory factors like TNF-α and IL-1β secreted by M1 macrophages inhibited the osteogenesis *in vitro*. On the contrary, under inflammatory conditions, the immune microenvironment modulated by J-CeM@Au nanomotor exhibited reduced expression of TNF-α and IL-1β but increased production of IL-10, thereby enhancing the osteogenic differentiation of hPDLSCs. In
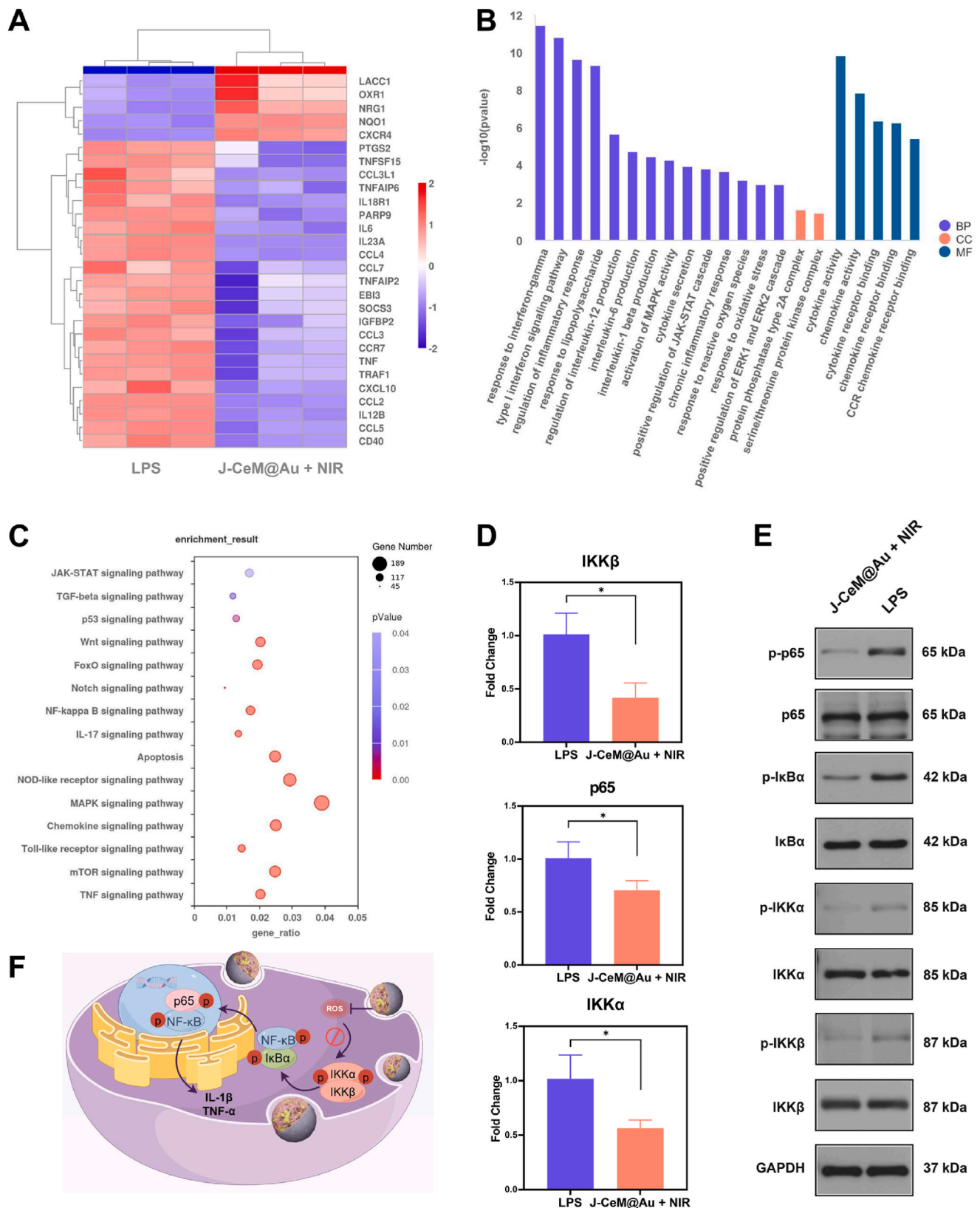
Fig. 5. *In vitro* modulatory mechanism of macrophage polarization induced by NIR-activated J-CeM@Au. (A) Heatmap analysis of differentially expressed genes involved in macrophage polarization after J-CeM@Au + NIR treatment. (B) GO analysis of genes in macrophages treated by J-CeM@Au + NIR versus LPS. BP, biological processes; CC, cellular components; MF, molecular functions. (C) KEGG enrichment analysis for the identified differentially expressed genes of two groups. (D) RT-qPCR results of IKKα, IKKβ, p65 mRNA expression in two groups. (E) WB results of the expression level of key proteins on NF-κB pathway. (F) Schematic illustration of the mechanism of M1-to-M2 macrophage transition induced by NIR-activated J-CeM@Au via inhibition of NF-κB signaling pathway.
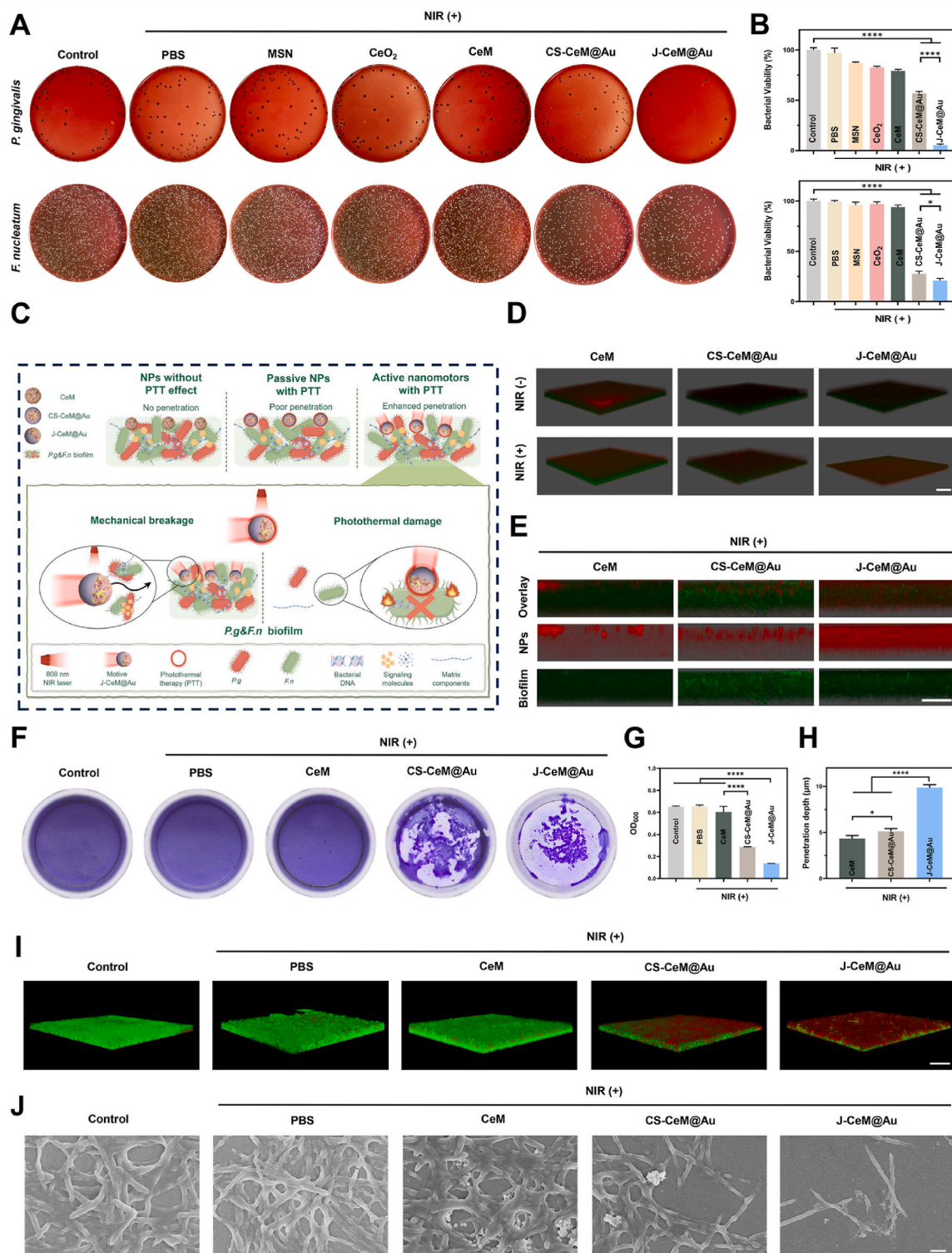
Fig. 6. *In vitro* antibacterial effect against planktonic *F. n* and *P. g*, penetration and antibacterial effect on *P.g & F.n* dual-species biofilms. (A) Representative photographs and (B) Analysis of bacterial viability on agar plate by plate dilution method. (C) Schematic illustration for the anti-biofilm ability of J-CeM@Au by enhanced biofilm penetration and PPT effects under NIR irradiation. (D) Images of 3D CLSM showing NPs (red) penetration into biofilms (green) before and after NIR irradiation. Scar bar = 50 μm. (E) Representative z-stack CLSM photos illustrating the distribution of NPs (red) and biofilms (green) and (H) quantification of penetration depth after NIR irradiation. Scar bar = 25 μm. (F) Crystal violet staining and (G) relative quantification of biofilm biomass under different treatments. (I) Images of 3D CLSM of Live/Dead staining of biofilms by SYTO 9 and PI. Scale bar = 50 μm. (J) SEM photos of biofilms after different treatments. Scale bar = 1 μm.

summary, these results indicated that the J-CeM@Au nanomotor has the potential to regulate the immune response of macrophages and subsequently promote impaired osteogenesis in an inflammatory condition.

2.5. In vitro immunomodulatory mechanism of J-CeM@Au

To elucidate the underlying mechanism of NIR-activated J-CeM@Au on macrophage polarization in the presence of LPS, RNA sequencing of THP-1-derived macrophages was performed. Volcano plot (Fig. S9B) showed that among the 622 differentially expressed genes, 241 genes were upregulated, and 381 genes were downregulated. The Venn diagram (Fig. S9C) demonstrated that 11585 genes were shared by two groups, while 811 genes were exclusively expressed in NIR-activated J-CeM@Au group and 768 genes were exclusively expressed in the LPS group. Furthermore, transcriptome analysis (Fig. 5A) revealed both upregulation and downregulation of inflammation-related genes in two groups. The upregulation of antioxidant genes like human oxidation resistance 1 (OXR1)/NAD(P)H quinone oxidoreductase 1 (NQO1) and anti-inflammatory genes such as neuregulin 1 (NRG1)/C-X-C motif chemokine receptor 4 (CXCR4) in the NIR-activated J-CeM@Au group might contribute to shielding against oxidative damage and reducing inflammation in LPS-stimulated macrophages. On the other hand, pro-inflammatory genes associated with M1 macrophages polarization such as CCL2, CCL3, CCL4, CCL5, CCL7, CCR7, CXCL10, IL-6, and TNF, were downregulated in the NIR-activated J-CeM@Au group compared to the LPS-treated group, indicating the immunomodulatory effects of NIR-activated J-CeM@Au in inhibiting M1 macrophage polarization during periodontitis.

Based on these differently expressed genes, gene ontology (GO) enrichment analysis (Fig. 5B) was performed on three gene ontology categories: biological processes (BP), cellular components (CC), and molecular functions (MF). The results showed that regulation of inflammatory response, response to LPS, activation of mitogen-activated protein kinases (MAPK) activity, chronic inflammatory response, response to ROS, cytokine and chemokine activity, receptor ligand activity etc., were closely related to macrophage polarization induced by NIR-activated J-CeM@Au during inflammation.

To further evaluate the potential signal transduction pathways, Kyoto Encyclopedia of Genes and Genomes (KEGG) pathway enrichment analysis (Fig. 5C) was performed. The results indicated that TNF signaling pathway, Toll-like receptor signaling pathway, MAPK signaling pathway, NF-κB signaling pathway were highly associated with the down-regulated M1 macrophage polarization by NIR-activated J-CeM@Au. Additionally, TGF-β signaling pathway may be involved in the enhanced M2 macrophage polarization. Moreover, J-CeM@Au nanomotor also influenced oxidative stress-related pathways including adenosine 5′-monophosphate (AMP)-activated protein kinase (AMPK) signaling pathway and Notch signaling pathway.

Among the differentially expressed pathways revealed by KEGG enrichment analysis, the NF-κB signaling pathway plays a crucial role in connecting antioxidant stress with macrophage polarization [59]. The activation of NF-κB, induced by excessive ROS and inflammatory mediators like TNF-α, leads to a pro-inflammatory state and M1-like macrophage polarization [60]. To confirm the underlying mechanism of the *in vitro* anti-inflammatory effect of J-CeM@Au nanomotor on LPS-treated macrophages, RT-qPCR and Western blot (WB) assays were performed to detect the key signal molecules in the NF-κB signal pathway to confirm our hypothesis on the basis of RNA-sequencing results. Fig. 5D showed that the mRNA expression of inhibitor of κB (IκB) kinase alpha (IKKα), IκB kinase beta (IKKβ) and NF-κB p65 (p65) was down-regulated in NIR-activated J-CeM@Au group. In addition, the protein expression of phosphorylation p65 (*p*-p65), phosphorylation of IκB kinase alpha and beta (*p*-IKKα and *p*-IKKβ), and phosphorylation of IκB alpha (*p*-IκBα) were inhibited by J-CeM@Au nanomotor compared to LPS-primed group, as shown in Fig. 5E. These findings indicated that J-CeM@Au nanomotor suppressed the pro-inflammatory state by

inhibiting the NF-κB signaling pathway. In conclusion, the ROS-scavenging J-CeM@Au nanomotor can modulate the macrophage polarization from pro-inflammatory M1 to anti-inflammatory M2 phenotype by inhibiting the NF-κB pathway in an LPS-induced inflammatory microenvironment *in vitro*. The schematic diagram illustrating the molecular mechanism is presented in Fig. 5F.

2.6. In vitro anti-planktonic bacterial ability

Two periodontal pathogens, *P. g* and *F. n* were chosen to investigate the anti-planktonic bacterial ability of NIR irradiated J-CeM@Au NPs, since they are key pathogens and play a crucial role in the initiation and progression of periodontitis [61]. The effects of NPs on bacterial viability were evaluated by spread plate method and measuring the absorbance of bacterial suspensions at OD$_{600}$. Fig. S10 indicated that in the absence of NIR light, CeM, CS-CeM@Au and J-CeM@Au can hardly kill bacteria. Therefore, the groups of NPs without NIR light irradiation were excluded in the subsequent experiments. As shown in Fig. 6A and B, bacterial viability decreased to approximately 57 % for *P. g* and 28 % for *F. n* in CS-CeM@Au + NIR group, compared to the control group. Furthermore, in the NIR-activated J-CeM@Au group, bacterial viability significantly dropped to around 5 % for *P. g* and 21 % for *F. n*, in comparison to the control group. The results indicated that the J-CeM@Au nanomotor possessed a desirable antibacterial property against periodontal pathogenic bacteria due to its superior photothermal effect with the help of active motion. Live/dead staining (Fig. S11A) revealed a significant decrease in the number of living bacterial cells (green) and an increase in the number of dead bacterial cells (red) in the J-CeM@Au + NIR group. Next, scanning electron microscope (SEM) was employed to detect membrane damage of bacteria after different treatments. As observed in Fig. S11B, the bacteria in the Au-free groups exhibited nearly intact morphology and smooth membranes similar to the control group. However, in J-CeM@Au + NIR group, severe cell membrane destruction and shrinkage of bacterial cells (red arrows) were observed, suggesting that the photothermal effects of J-CeM@Au induced a potent antibacterial response against on *P. g* and *F. n* [62]. Overall, these results collectively demonstrated that J-CeM@Au NPs possessed an effective *in vitro* antibacterial capability under NIR laser irradiation, which may be attributed to the superior photothermal effect under active motion.

2.7. In vitro penetration of J-CeM@Au into biofilms

In the context of periodontitis, deep-seated pathogens usually form microbial aggregates known as dental biofilms, to resist the attack of host immunity and antibacterial agents [63]. Biofilms, in contrast to planktonic bacteria, are composed of extracellular polymeric substances (EPS), secretions, bacterial organisms, and other components [64]. Biofilms exhibit strong adherence to both abiotic surfaces, such as dentures, and biotic surfaces, including teeth and mucosae, which are difficult to access and eliminate [65]. Intractable biofilms cause persistent infections and bring about challenges for anti-infection treatment. Therefore, it is crucial to thoroughly investigate the anti-biofilm capacity of nanoagents in addition to their bactericidal effects against planktonic bacteria.

To date, various types of biofilm models have been utilized in periodontitis-related researches. Multispecies biofilms are considered more representative and practical compared to single-species biofilms since subgingival dental plaques are composed of multiple species of bacteria [66]. It would be significant and challenging to eliminate multispecies biofilms in terms of evaluating the anti-biofilm capacity of NPs. In consequence, a dual-species biofilm consisting of *P. g* and *F. n* was employed as a model in the subsequent experiments, as these bacteria are keystone pathogens and crucial for the initiation and maturation of periodontal biofilms.

The anti-biofilm mechanism of J-CeM@Au against *P. g* and *F. n* biofilm is illustrated in Fig. 6C. Prior to verifying the antibiofilm effect of
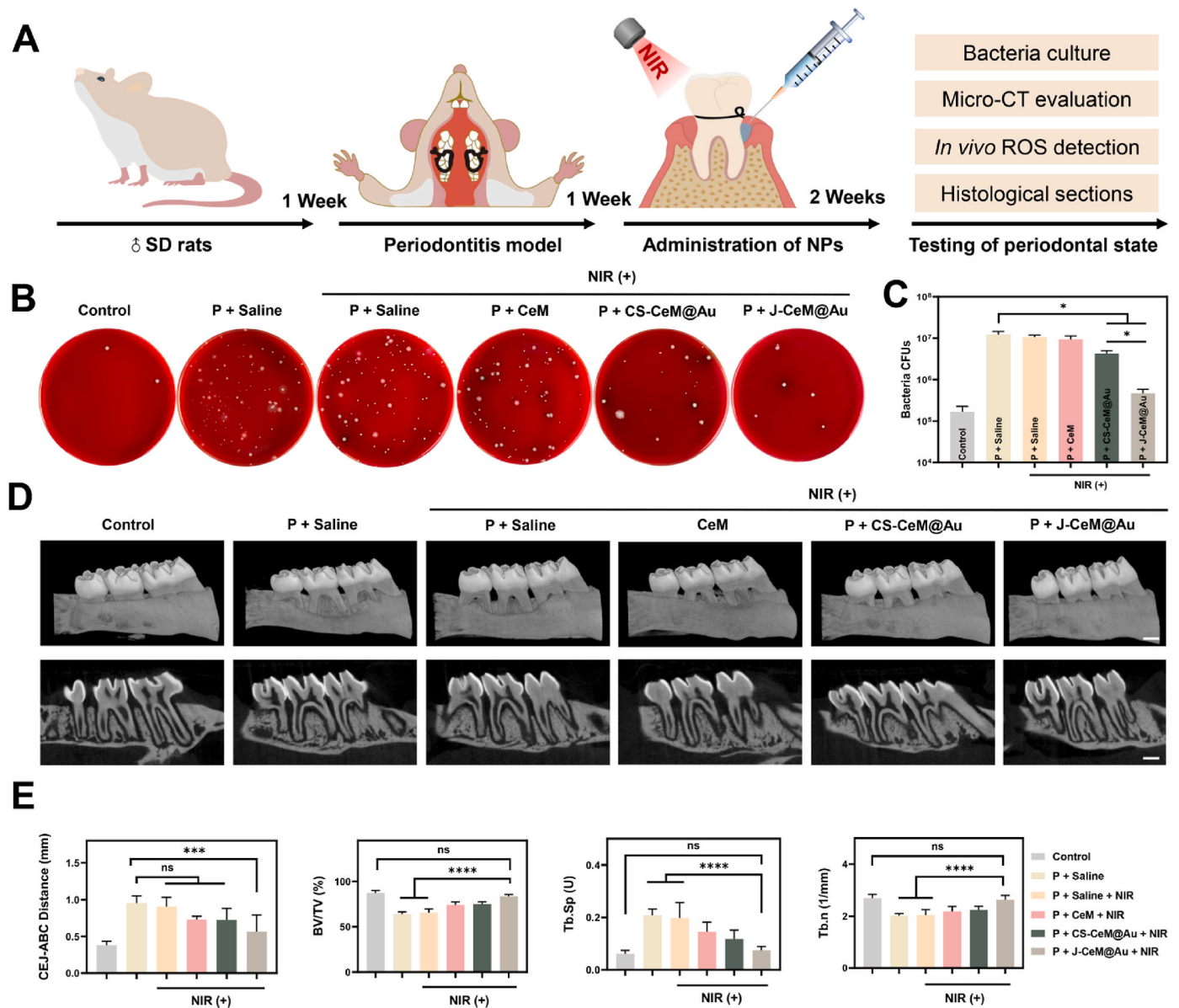
Fig. 7. *In vivo* anti-bacterial and antiresorptive effects on rats with periodontitis. (A) Schematic image of animal experiments. (B) CFUs of bacteria isolated from periodontal pockets on agar plates with the dilution of 10^5. (C) Corresponding quantification of bacteria CFUs in different groups. (D) 3D reconstruction and bucco-palatal section graphs of maxillary molar and alveolar bone by micro-CT scanning. Scale bar = 1 mm. (E) Quantification of the buccal CEJ-ABC distance, BV/TV, Tb. Sp, Tb. n in different groups.

the Janus nanomotor, the penetration ability and accumulation effects of J-CeM@Au were assessed. CeM, CS-CeM@Au and J-CeM@Au were fluorescent labeled with Cyanine3 (Cy3) (red), and then incubated with the biofilms which were stained with SYTO9 (green). Fluorescence imaging was used to track the locations of CeM, CS-CeM@Au, and J-CeM@Au in biofilms before and after NIR irradiation. As shown in Fig. 6D, only weak red fluorescence was observed in biofilm treated with CeM and CS-CeM@Au. In contrast, strong red fluorescence appeared throughout the biofilm treated by J-CeM@Au nanomotor. Z-stack imaging (Fig. 6E) was employed to visualize the distribution of the NPs. Following NIR irradiation, CeM and CS-CeM@Au NPs remained almost on the surface of the biofilms. However, J-CeM@Au nanomotors could penetrate nearly the entire layer of biofilm. The penetration depth of J-CeM@Au was the greatest of all the groups (Fig. 6H).

As previously discussed, the intricate architecture of biofilms has significantly influenced the therapeutic efficacy of antibacterial agents over the years. To address this issue, promoting drug penetration and

inhibiting EPS interference are two primary strategies for combating biofilm infections [64]. To overcome the EPS barriers, passive methods like morphology control, electrostatic interaction and targeted modification are usually employed to modify the nanomaterials to disrupt the EPS [67]. However, the effectiveness of these passive methods in biofilm removal remains limited. Recently, an active strategy by applying an external force to propel the antibacterial agents toward the deep layers of biofilms has garnered attention from researchers. In this scenario, nanoagents convert external energy, such as chemical, optical, and acoustic energy, into mechanical energy, thereby disrupting the biofilm matrix and facilitating antibacterial effects [68].

Our study demonstrated that the active J-CeM@Au nanomotor propelled by NIR exhibited superior penetration ability compared to the passive CS-CeM@Au and CeM NPs. This suggests that the mechanical impact and photothermal damage produced by J-CeM@Au facilitated the enhanced penetration of the biofilm matrix. Collectively, the results inspire us to design motive nanomotors instead of passive NPs to actively
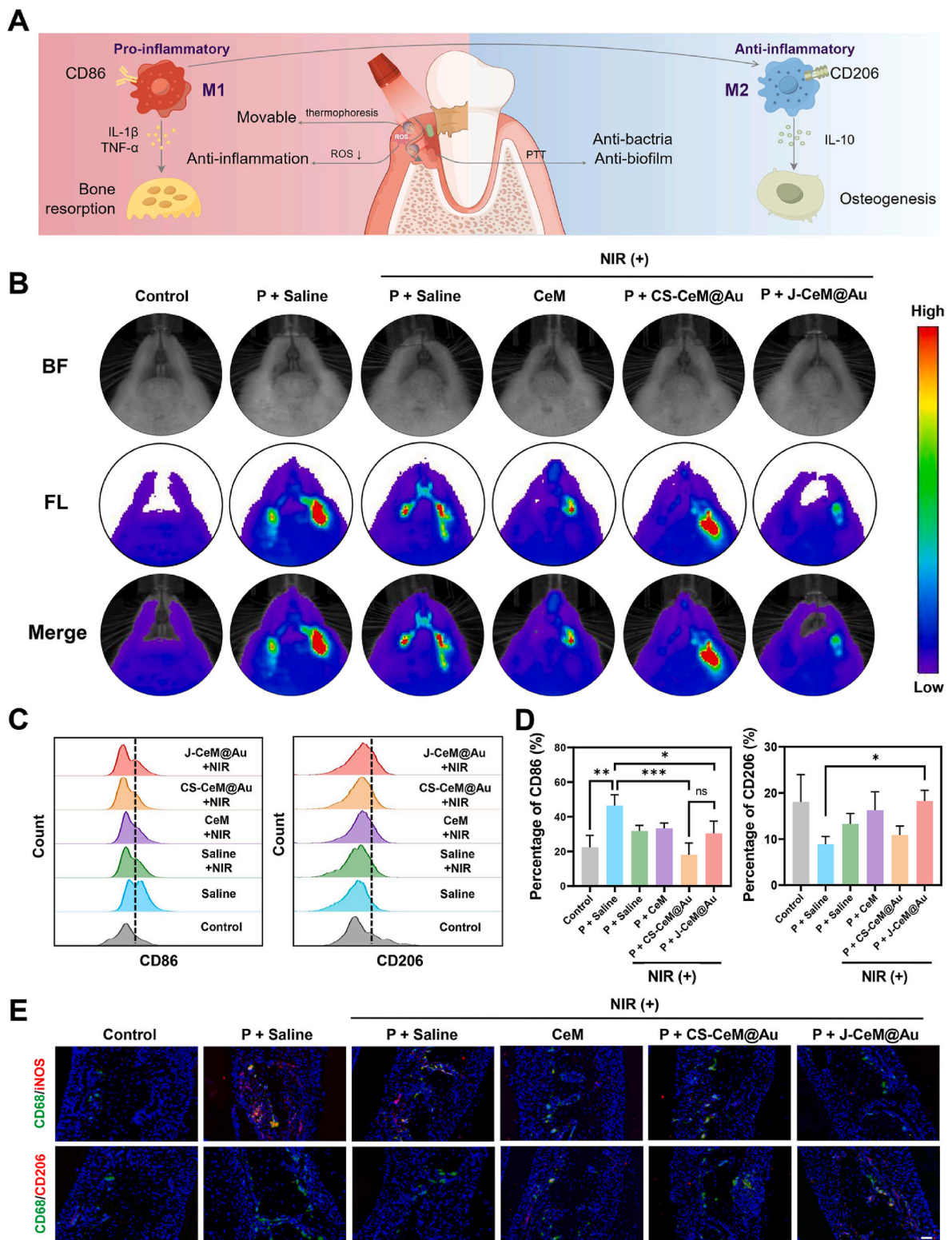
Fig. 8. *In vivo* ROS-scavenging and immunomodulation effects around second molars in rats with periodontitis. (A) Schematic diagram of enhanced ROS-scavenging efficacy and resultant M1-M2 macrophage transition induced by J-CeM@Au nanomotor in periodontitis. (B) *In vivo* fluorescence imaging of ROS in periodontal areas of different groups. (C) Representative flow cytometry histograms and (D) quantification of surface markers (CD86 and CD206) expression of macrophages (CD68$^+$ and CD11b/c$^+$) isolated from periodontal soft tissue. (E) Immunofluorescence staining of macrophage markers CD68/iNOS (M1) and CD68/CD206 (M2) in the alveolar bone. Scale bar = 50 μm.
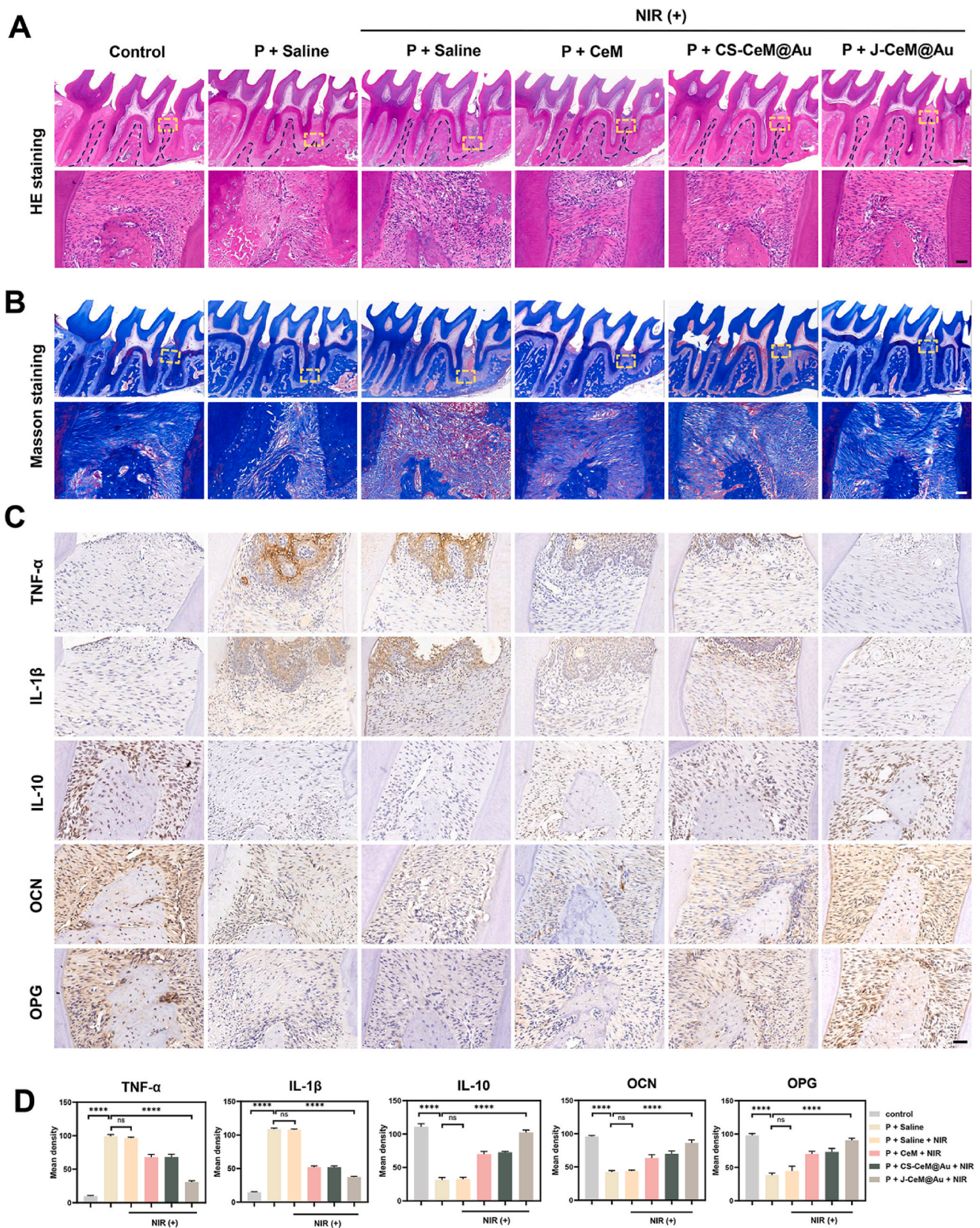
Fig. 9. Histological evaluation of periodontal tissues around second molars. (A) HE staining of paraffin sections of periodontal tissues around second molars. The scale bars represent 500 μm for the unmagnified image (upper row) and 50 μm for the magnified image (lower row). (B) Masson's trichrome staining of periodontal tissues around second molars. The scale bars represent 500 μm for the unmagnified image (upper row) and 50 μm for the magnified image (lower row). (C) Expression of TNF-α, IL-1β, IL-10, OCN, OPG by immunohistochemical staining of periodontal tissues around second molars and (D) quantitative analysis. Scale bar = 50 μm.

overcome the biofilm matrix barrier in the context of biofilm treatment.

2.8. In vitro biofilm elimination effects

The anti-biofilm efficacy of NIR-activated CS-CeM@Au and J-CeM@Au was further tested. Crystal violet staining of the biofilms (Fig. 6F) and its quantification (Fig. 6G) showed there were intact purple-stained biofilms in Au-free groups but destroyed to the most extent in NIR-activated J-CeM@Au group. As shown in Fig. 6I, live/dead staining of the biofilms showed that Au-free groups exhibited dense and intact biofilms with green fluorescence, while the NIR-activated J-CeM@Au group displayed sparse and red-stained biofilms. Meanwhile, the morphology changes of biofilm on the glass surface were observed by SEM (Fig. 6J). The bacterial aggregate in the control group was dense and intact, while its density decreased in the NIR-activated J-CeM@Au group. The photothermal effect can result in bacterial membrane breakage and protein denaturation. Given that CS-CeM@Au shares similar photothermal property with J-CeM@Au but lacks mobility, it is rational for CS-CeM@Au to produce moderate clearance effect of biofilm with NIR laser irradiation. In the case of the J-CeM@Au nanomotor, with synergistic photothermal effects and thermophoresis, can break through the biofilm matrix and penetrate deep into the plaque to achieve biofilm clearance, resulting in only sporadic bacteria observed. Therefore, these results demonstrate that NIR-activated J-CeM@Au possesses the most effective biofilm elimination ability *in vitro*, inspiring the development of mobilizable PTAs for combating biofilm-related infections in the future. Several limitations exist in this study. Firstly, subgingival biofilms in periodontitis are significantly more complex and dynamic compared to the simplified and static *in vitro* biofilm models typically used in experiments. Additionally, the dual-species biofilms of *P. g* and *F. n* are susceptible to environmental stress due to the lack of polysaccharides and stress-responsive systems [69]. A multi-species dynamic model is expected to be employed in future researches to assess the anti-biofilm efficacy of NIR-activated J-CeM@Au, aligning more closely with the actual conditions present in periodontitis [70].

2.9. In vivo anti-bacterial effects and inhibition of bone resorption in periodontitis

Experimental periodontitis was established in rats by ligaturing silk and locally injecting *P. g* to evaluate the effectiveness of J-CeM@Au nanomotor. The treatment procedures and the placement of the silk ligatures on the second molars were depicted in Fig. 7A and Fig. S12A. The gingival cervical fluid was diluted and spread on plates for colony-forming units (CFUs) count. The results demonstrated a significant decrease in CFUs for the CS-CeM@Au and J-CeM@Au groups under NIR irradiation compared to the periodontitis group (Fig. 7B and C). Remarkably, the NIR-activated J-CeM@Au group exhibited a significantly greater reduction in CFUs compared to the CS-CeM@Au group. The CFUs of CeM-treated periodontitis group remained nearly unchanged compared to the saline-treated periodontitis groups with or without NIR irradiation. Collectively, NIR-activated J-CeM@Au exhibited excellent antibacterial properties *in vivo*.

Alveolar bone remodeling involves bone formation phase and bone resorption phase in the periodontium [71]. While in periodontitis, the homeostasis of bone remodeling is broken because of the elevated receptor activator of nuclear factor-κB ligand (RANKL)/osteoprotegrin (OPG) ratio mediated by ROS in the local inflammatory environment, resulting in continuous bone resorption [72]. To further evaluate the extent of alveolar bone resorption around the second molars, the harvested maxillae were scanned by micro-computed tomography (micro-CT). As seen in Fig. 7D, the 3D reconstruction images and bucco-palatal section graphs of maxillae showed the severe buccal alveolar bone resorption in saline-treated periodontitis groups compared to the control group. However, the bone resorption was alleviated by CeM and CS-CeM@Au under NIR irradiation, possibly due

to the ROS-scavenging efficiency of CeO$_2$ and the photothermal antibacterial effects of Au. The alveolar bone loss in the J-CeM@Au-treated group under NIR irradiation was less compared to the CS-CeM@Au treated group, which was due to the superior antibacterial and ROS-scavenging capacity endowed by the active motion of the nanomotor. Alveolar bone resorption was quantified by measuring the distance between the cementoenamel junction and the alveolar bone crest (CEJ-ABC), which was significantly decreased in the J-CeM@Au-treated group under NIR irradiation (Fig. 7E). The bone volume to total volume ratio (BV/TV), trabecular spacing (Tb. Sp) and trabecular number (Tb. n) were higher in the J-CeM@Au-treated group compared to the saline-treated periodontitis groups (Fig. 7E). These results indicated that NIR-activated J-CeM@Au not only alleviated gingival inflammation, but also relieved alveolar bone resorption in periodontitis.

2.10. In vivo anti-oxidative and anti-inflammatory effects

The *in vivo* anti-oxidative and anti-inflammatory effects of J-CeM@Au nanomotor were illustrated in Fig. 8A. At the end of treatment procedure (2 weeks post-establishment of periodontitis), the *in vivo* ROS-scavenging ability of J-CeM@Au nanomotor was evaluated by injecting DCFH-DA, a fluorescent probe for ROS, into the periodontal pockets and detecting the fluorescence signal with an *in vivo* fluorescence imaging system [73]. Fig. 8B illustrated a pronounced fluorescence signal at the periodontal sites in the saline-treated periodontitis groups, in contrast to the minimal fluorescence observed in the healthy control. Nevertheless, the fluorescence signal slightly decreased in the CeM and CS-CeM@Au groups, indicating partial alleviation of inflammation. Surprisingly, the NIR-activated J-CeM@Au group exhibited a significantly reduced fluorescence intensity, potentially due to the enhanced ROS-scavenging efficiency and antimicrobial activity induced by flexible movement.

The rats were then sacrificed to confirm the immunomodulatory activity exerted by NIR-activated J-CeM@Au during the progression phase of periodontitis, flow cytometry (FCM), immunofluorescence (IF) staining and immunohistochemical (IHC) staining were used to evaluate polarization state of macrophages in the periodontal tissues. Initially, we analyzed the polarization state of macrophages in gingival tissues using FCM, in which cells co-expressing CD68 and CD11b/c were identified as macrophages. As shown in Fig. 8C and D, under NIR irradiation, the percentage of CD206-positive M2 macrophages in J-CeM@Au-treated group was significantly higher compared with saline-treated periodontitis groups. Moreover, the population of CD86-positive M1 macrophages was significantly reduced in both the CS-CeM@Au-treated group and the J-CeM@Au-treated group compared to the saline-treated periodontitis groups. These results indicate that NIR-activated J-CeM@Au can relieve gingival inflammation *in vivo*.

For IF staining, CD68 (green) was used as a pan-macrophage marker. CD206 (red) and iNOS (red) fluorescence staining was performed to identify M2 macrophages and M1 macrophages, respectively. Fig. 8E showed a significant infiltration of CD68$^+$iNOS$^+$ M1 macrophages in the saline-treated periodontitis groups, indicating a pro-inflammatory state. Nevertheless, co-expression of CD68 and iNOS in the J-CeM@Au-treated group under NIR irradiation was lower compared to periodontitis groups, suggesting a lower presence of M1 macrophages in the affected area. On the other hand, the saline-treated periodontitis groups showed a low presence of CD68$^+$CD206$^+$ M2 macrophages, while the J-CeM@Au-treated group under NIR irradiation exhibited a significant number of double-stained M2 macrophages, indicating that NIR-activated J-CeM@Au could promote macrophages polarization from M1 to M2 phenotype.

2.11. Histological assessment for therapeutic effects in vivo

Further histological assessment was conducted to evaluate therapeutic effects of J-CeM@Au in periodontitis. Representative hematoxylin-eosin (H&E) staining (Fig. 9A) of the maxillary tissues

revealed that in saline-treated periodontitis group, the junctional epithelium was attached distally to CEJ with abundant infiltration of inflammatory cells, and the alveolar bone was resorbed almost to the apical third (dotted line). Alveolar bone loss was partially relived by CeM and CS-CeM@Au under NIR irradiation, as evidenced by the greater alveolar ridge heights compared to the periodontitis group. Notably, NIR-activated J-CeM@Au effectively prevented alveolar bone resorption, leading to significant recovery of the alveolar ridge height. Subsequent Masson's trichrome staining revealed the presence of degenerated and deteriorated fibers in the saline-treated periodontitis groups (Fig. 9B). However, elastic fibers and collagenous fibers exhibited greater density and well organization in NIR-activated J-CeM@Au group, resembling the normal tissue in the control group. The deposited collagens can serve as fibrous scaffolds for mineral deposition, thereby promoting cementum and new bone formation by progenitor cells in periodontal tissue [74].

Furthermore, IHC staining and quantitative analysis (Fig. 9C and D) revealed elevated expression levels of the pro-inflammatory factors TNF-α and IL-1β in the saline-treated periodontitis groups, indicating the presence of severe gingival inflammation in periodontitis. However, upon NIR irradiation, the J-CeM@Au-treated group exhibited a significant reduction in the expression of TNF-α and IL-1β, indicating the remarkable anti-inflammatory effect. Additionally, Ce-containing NPs enhanced the expression of anti-inflammatory cytokine IL-10, with the most pronounced effect observed in the NIR-activated J-CeM@Au group. Furthermore, osteogenic differentiation-related factors, osteocalcin (OCN) and OPG, were highly expressed in J-CeM@Au-treated group, in comparison to other periodontitis groups. In conclusion, the NIR-activated J-CeM@Au demonstrated the potential to mitigate periodontal inflammation and promote alveolar bone osteogenesis through the modulation of M2 macrophage polarization.

2.12. In vivo biosafety assessment

To assess the biosafety of the NPs *in vivo*, H&E staining of tissue sections from major organs including the heart, liver, spleen, lung, and kidney, was initially performed. As shown in Fig. S13, no pathological necrosis and inflammation lesions were found in the experimental and control groups. The body weight curve throughout the experimental period was plotted in Fig. S12B and no abnormal changes were seen in the experimental groups, indicating negligible toxicity of NPs *in vivo*. Hematology and serological markers, as shown in Fig. S14, were analyzed, including white blood cells (WBC), lymphocytes (Lymph), intermediate cells (Mid), neutrophile granulocyte (Gran), total proteins (TP), albumin (ALB), globulin (GLO), red blood cells (RBC), total bilirubin (TBIL), aspartate aminotransferase (AST), alanine aminotransferase (ALT), creatinine (CRE) and urea. The results demonstrated that J-CeM@Au exhibited no adverse immune response (WBC, Lymph, Mid, Gran, TP, ALB and GLO), cytotoxicity (RBC), hepatotoxicity (TBIL, AST, and ALT), renal toxicity (CRE, urea) in rats compared to the control group.

3. Conclusion

In this study, we have fabricated J-CeM@Au nanomotors propelled by NIR laser, which exhibit improved antioxidant and anti-biofilm capabilities. Within the microenvironment of periodontitis, J-CeM@Au nanomotor effectively eliminates the biofilm of periodontal pathogens, consequently reducing the burden of external toxins. Additionally, the J-CeM@Au nanomotor can actively scavenge excess ROS, alleviating local inflammation by inducing the transition of M1-to-M2 macrophages through the NF-κB signaling pathway, which creates a favorable environment for subsequent periodontal regeneration by promoting osteogenic differentiation of hPDLSCs. In summary, based on the results of this study, the multipronged tactics harnessing the autonomous motion propelled by NIR to improve antioxidation, antibiofilm capacity and

immunomodulation of the J-CeM@Au nanomotor was proved to be practical in periodontitis treatment. Moreover, our strategy holds potential for the treatment of other inflammatory diseases caused by bacterial infections, such as peri-implantitis and osteomyelitis.

4. Materials and methods

4.1. Materials and reagents

Triethanolamine (TEA), Sodium salicylate (NaSal), Cetyltrimethylammonium Bromide (CTAB), Tetraethyl orthosilicate (TEOS), (3-aminopropyl) triethoxysilane (APTES), 2-Bromo-2-methylpropionic acid (BMPA), N, N-dimethylformamide (DMF), Cyanine3 NHS easter (Cy3) were purchased from Aladdin Reagent (Shanghai, China). Phorbol 12-myristate 13-acetate (PMA) was purchased from MedChemExpress (MCE, USA).

4.2. Preparation of MSNs

Dendritic MSNs was synthesized according to previous studies. Briefly, TEA (136 mg) was dissolved in ddH$_2$O (50 mL) at 80 °C with magnetic stirring for 0.5 h. Then, NaSal (336 mg) and CTAB (570 mg) were added and the mixture was stirred for an additional 1 h at 80 °C. Subsequently, TEOS (8 mL) was added dropwise into the solution, and the mixture was gently stirred for 2 h. The products were collected by centrifugation (4000 rpm, 15 min) and washed three times with water and ethanol to remove the residual reactants. The final products were extracted three times with a 10 % methanolic HCl solution at 80 °C for 6 h each time to remove the surfactants (CTAB), and then dried overnight at 80 °C under vacuum.

4.3. Preparation of MSN-NH$_2$

Dried MSNs (0.2 g) and methanol (50 mL) were added to a round bottom flask and stirred for 0.5 h. Then, APTES (1 mL) was added, and the mixture was refluxed at 80 °C for 12 h. The product was washed with ethanol and water, and then then centrifuged at 4000 rpm for 15 min. After centrifugation, it was dried under vacuum at 60 °C overnight.

4.4. Preparation of CeO$_2$ NPs and BMPA-capped CeO$_2$ NPs

Nano ceria was synthesized following previously reported methods [75]. In brief, cerium (III) acetate (0.43 g) and oleylamine (3.2 g) were added to xylene (15 mL) and stirred at room temperature for 2 h. The reaction solution was then heated to 90 °C, and 1 mL ddH$_2$O was added under vigorous stirring. The reaction was further continued at 90 °C with vigorous stirring for 3 h. The resulting yellow colloidal solution was then cooled to room temperature. CeO$_2$ NPs were precipitated by adding 100 mL of ethanol to the solution. The product was washed several times with ethanol and ddH$_2$O. The synthesized nano ceria was stored in 20 mL of n-hexane. BMPA (0.5 g) and citric acid (0.05 g) were dissolved in DMF (15 mL). Then, 15 mg of the synthesized CeO$_2$ NPs were added to the above solution and stirred at 30 °C for 6 h to synthesize BMPA-capped CeO$_2$ NPs.

4.5. Preparation of CeM NPs

Swiftly, 2 mL of the MSN-NH$_2$ dispersion (5 mg/mL) was added to 10 mL of BMPA-capped CeO$_2$ NPs dispersion (1 mg/mL). Subsequently, the mixture was stirred at room temperature for 6 h. The resulting CeO$_2$-loaded MSN (CeM) was retrieved by centrifugation and washed for several times with ethanol and ddH$_2$O.

4.6. Preparation of J-CeM@Au NPs

J-CeM@Au NPs were synthesized using the sputter coating method

[76]. Briefly, the as-prepared CeM NPs were dispersed in an ethanol solution, then dropped onto a hydrophilic silicon wafer to form a monolayer structure, and subsequently dried under vacuum. A hemispheric gold layer was deposited on the upper half surface of the CeM using an ion sputtering instrument (JFC 1600, JEOL Ltd., Japan) through chemical vapor deposition. Finally, the J-CeM@Au NPs were released from the silicon wafer through gentle ultrasonic treatment, and then fluorescence-functionalized with Cy3 for microscopy observations.

4.7. Preparation of CS-CeM@Au NPs

Core-shell CeM coated with Au (CS-CeM@Au) was prepared for comparison by seed-mediated growth [77]. In short, AuNPs were firstly synthesized by adding 6 μL of THPC (80 % aqueous solution) and 0.75 mL of NaOH (0.2 M) into 23.75 mL ddH$_2$O with vigorous stirring at 25 °C for 5 min. Subsequently, 0.5 mL of HAuCl$_4$ (20 mg/mL) was added to the mixture and stirred vigorously for 30 min. The stock solution was stored at 4 °C for 3 days before use. Secondly, MSN-NH$_2$ (2 mg) was dispersed in a 10 mL suspension of AuNPs using sonication for 20 min. The mixture was then placed on a shaking table overnight. The products were retrieved by centrifugation, washed for several times with ethanol and ddH$_2$O, and then resuspended in 2 mL PVP solution (1 mg/mL) to obtain CeM@Au seeds. Finally, 200 μL of CeM seeds (1 mg/mL) and 10 mg of PVP were added to 9.8 mL ddH$_2$O with stirring. Then, 20 μL of HAuCl$_4$ (10 mM) and 40 μL of ascorbic acid (10 mM) were added with stirring for 15 min to reduce Au^{3+} to Au nanoparticle. The reduction procedure was repeated twice.

4.8. Characterization

Nanoparticle morphologies were observed using a transmission electron microscopy (TEM, JEOL, JEM-F200, Japan) equipped with an energy dispersive spectroscopy (EDS). X-ray diffraction patterns were analyzed by an X-ray diffractometer (XRD, Rigaku, Smartlab SE, Japan) with Cu-Kα radiation. The particle size was measured by dynamic light scattering (DLS, Malvern Zetasizer, ZEN3600, UK), and the zeta potential value was determined. X-ray photoelectron spectroscopy (XPS) was performed using an ESCALAB 250XI spectrometer (Thermo Scientific, USA). Elemental analysis of Ce ions was performed by an inductively coupled plasma mass spectrometry (ICP-MS, PQ-MS, Analytik Jena, Germany).

4.9. Evaluation of ROS-scavenging abilities

The total antioxidant activity of synthesized NPs was determined using the Total Antioxidant Capacity Assay Kit (Beyotime, China) according to the manufacturer's instructions. Additionally, the total antioxidant activity of J-CeM@Au was evaluated using an 808 nm NIR laser (Beijing Laserwave OptoElectronics Technology Co., Ltd) to evaluate the ROS-scavenging efficiency of the Janus nanomotor. The catalase (CAT)-like catalytic activity was determined using the Catalase Assay Kit (Beyotime, China) according to the provided instructions. The Superoxide Dismutase (SOD)-like catalytic activity was measured by the Total Superoxide Dismutase Assay Kit with WST-8 (Beyotime, China).

4.10. Evaluation of photothermal properties

The thermal properties of synthesized NPs under 808 nm NIR irradiation (0.0–3.0 W/cm^2) were evaluated using an infrared thermal imager (Beijing JCHY Technology Co., Ltd, JIR-A384, China). Initially, 0.2 mL suspensions of H$_2$O, MSN (400 μg/mL), CeO$_2$ (27 μg/mL), CeM (133 μg/mL), CS-CeM@Au (400 μg/mL), J-CeM@Au (400 μg/mL) in 1 mL plastic centrifugal tubes were irradiated with an 808 nm NIR laser (1 W/cm^2) to obtain the thermographs and temperature-time curves. Subsequently, the photothermal stability of J-CeM@Au (400 μg/mL) was assessed by recording five cycles of heating and cooling processes

under a 1 W/cm^2 laser, and the compelete heating and cooling curve was plotted. Finally, the temperature changes were recorded for different concentrations (100, 200, 400, 800 μg/mL) of J-CeM@Au suspensions and laser intensities (1, 1.5, 2 W/cm^2).

4.11. Thermophoresis of J-CeM@Au

Fluorescence microscopy (IX83, Olympus Corporation, Japan) was utilized to observe the thermophoresis of the Cy3 labeled J-CeM@Au nanomotors. An independent laser system (Laserwave, Beijing, China) was employed for 808 nm NIR irradiation, and the optical probe was fixed to ensure that the laser beam was vertically directed onto the sample plane. The J-CeM@Au nanomotors were placed in a covered Petri dish containing an aqueous solution to minimize the drift effect. Each video capturing the movement of J-CeM@Au was recorded using a camera while the nanomotors were continuously irradiated with a laser (0.0–3.0 W/cm^2). The movies were recorded at a frame rate of 12 frames per second, and 15 individual particles were tracked two-dimensionally for 10 s. The tracking data were used for mathematical statistics and motion analysis. The videos were analyzed using the MTrack2 plugin for Fiji to record the X and Y coordinates of the nanomotors. The mean-square displacement (MSD) curves and diffusion coefficient were extracted from recorded trajectories using an open-source code for MATLAB 7.0. Finally, the data was exported and then plotted by Origin 2023.

4.12. Cell culture

THP-1 cells were obtained from GuangZhou Jennio Biotech Co., Ltd. THP-1 cells were cultured in RPMI 1640 medium (Gibco, USA) supplemented with 10 % fetal bovine serum (FBS, Gemini, USA) and 1 % penicillin-streptomycin (P/S, Gibco, USA) in 5 % CO$_2$ at 37 °C. To get THP-1-derived macrophages, the complete medium was supplemented with PMA (100 ng/mL) to induce cell adherence after 24 h. Human periodontal ligament stem cells (hPDLSCs) were obtained from patients with informed consent as previously described [49]. Briefly, periodontal ligament tissues from the middle third of the root surfaces of orthodontically extracted premolars were collected, washed with PBS, and cultured in α-MEM (HyClone, USA) supplemented with 15 % FBS (Gemini, USA) and 1 % P/S in 5 % CO$_2$ at 37 °C. hPDLSCs were isolated by selecting a single cell-derived colony. Cells at passages 3 to 6 (P3–P6) were used for subsequent experiments.

4.13. Cell proliferation

THP-1-derived macrophages were seeded in 96-well plates. After cell adherence, the media were supplemented with a series of concentrations (100, 200, 400, 800 μg/mL) of CeO$_2$, CeM, CS-CeM@Au, and J-CeM@Au NPs. Cell viability was assessed at 24 h and 48 h using a cell counting kit-8 (CCK-8, Dojindo, Japan), and the corresponding percentages were calculated.

4.14. Live/dead cell staining

Macrophages were seeded into 24-well plates. Following cell adherence, the medium was replaced with a medium containing NPs, with or without NIR irradiation for 5 min. After incubation for an additional 24 h, the cells were washed with PBS and stained with a commercial kit (Solarbio, China) containing CAM and PI, which indicated live and dead cells, respectively. Photographs were captured using an inverted fluorescence microscope (Olympus, Japan).

4.15. Cell apoptosis assay

Macrophages were seeded in 6-well plates. The attached cells were supplemented with NPs suspensions, with or without 808 nm NIR

irradiation for 5 min. After culturing for an additional 24 h, cell apoptosis was assessed using the Annexin V-FITC/PI Apoptosis Detection Kit (Vazyme, China). Briefly, cell samples were collected, washed twice, resuspended in a binding buffer, and stained with 5 μL of FITC Annexin V and PI for 10 min in the dark for flow cytometry analysis using Cytoflex (USA).

4.16. In-vitro ROS-scavenging assay

Macrophages were seeded in confocal dishes. The medium was supplemented with 1 μg/mL LPS from *P. g* to induce periodontal inflammation *in vitro* [78]. Following a 12-h stimulation, the LPS-containing medium was replaced with a complete medium containing MSN (400 μg/mL), CeO$_2$ (27 μg/mL), CeM (133 μg/mL), CS-CeM@Au (400 μg/mL) and J-CeM@Au (400 μg/mL). Subsequently, the cells were irradiated with NIR laser for 5 min. The cells cultured in a medium without LPS were used as the control group. After 24 h, the cells were incubated with a DCFH-DA probe (Beyotime, China) and observed using a laser scanning confocal microscope (FV1200, Olympus Corporation, Japan). The levels of intracellular ROS were quantitatively analyzed using Fiji software.

4.17. Macrophage polarization assay

Macrophages were seeded in 12-well plates and stimulated with LPS (1 μg/mL) for 12 h. The medium was then replaced with different NPs suspensions and irradiated with NIR laser for 5 min. After 24 h, the polarization state of macrophages was assessed using immunofluorescence staining, flow cytometry, and real-time quantitative polymerase chain reaction (RT-qPCR).

Prior to immunofluorescence staining, cells were washed with PBS and fixed with 4 % paraformaldehyde. Subsequently, macrophages were incubated overnight at 4 °C with rabbit anti-iNOS primary antibody (1:200 dilution, Abcam) and rabbit anti-IL-10 primary antibody (1:200 dilution, Abclonal). Thereafter, the cells were incubated at room temperature for 1 h with goat anti-rabbit DyLight594-conjugated IgG secondary antibody (1:200 dilution, Abbkine) and goat anti-rabbit DyLight488-conjugated IgG secondary antibody (1:200 dilution, Abbkine). Finally, the macrophages were stained with 4,6-diamino-2-phenylindole (DAPI, Beyotime) for 10 min in darkness to visualize the nuclei. Images of positively stained cells were captured using a fluorescence microscope (Olympus, Japan).

Cells were harvested from the plates for flow cytometry analysis, followed by centrifugation at 1000 rpm for 5 min and resuspension in PBS supplemented with 2 % FBS. Subsequently, macrophages were incubated with FITC-conjugated mouse anti-CD86 (1:100 dilution, Biolegend) and mouse anti-CD206 (1:100 dilution, Biolegend) antibodies. The stained cells were then detected with a Cytoflex flow cytometer (Beckman, USA), and the results were analyzed using CytExpert (Beckman, USA) and Flowjo (Tree Star, USA) softwares.

To confirm the mRNA expression of M1-related factors (TNF-α and IL-1β) and M2-related factors (Arg-1 and IL-10), macrophages were lysed, and total RNA was extracted by RNAiso Plus (Takara Bio, Japan). Subsequently, the cDNA was prepared by reverse transcription using the PrimeScript RT reagent Kit (Takara Bio, Japan). Finally, quantitative polymerase chain reaction (qPCR) was performed using the TB Green Premix Ex Taq II kit (Takara Bio, Japan) on the ABI QuantStudio6 system (Thermofisher, USA). Differential gene expression was analyzed using the $2^{-\Delta\Delta Ct}$ method. The sequences of primers were listed in Table S1.

4.18. Osteogenic differentiation of hPDLSCs by macrophage-conditioned medium

Macrophages were seeded in 12-well plates and stimulated with LPS for 12 h. The medium was then replaced with different NPs suspensions

and irradiated with NIR laser for 5 min. After 24 h, the supernatants from each group were collected and mixed with α-MEM medium at a volume ratio of 1:3. Subsequently, the medium was supplemented with 50 μg/mL ascorbic acid, 10 mM β-glycerophosphate, and 0.1 μM dexamethasone to prepare a macrophage-conditioned osteogenic differentiation medium (Mφ-CM), along with 10 % FBS and 1 % penicillin-streptomycin. The attached hPDLSCs were seeded in 24-well plates and cultured in Mφ-CM from different NPs. The Mφ-CM was refreshed every 2 days. On day 7, alkaline phosphatase (ALP) staining assay and ALP activity test were performed using NBT/BCIP ALP staining kits (Beyotime, China) and ALP Assay Kit (Beyotime, China), respectively, to analyze intracellular ALP expression levels according to the manufacture's description. Stained cells were photographed using a stereomicroscope (Leica, Germany). Additionally, an RT-qPCR assay was performed to assess the gene expression levels of osteogenesis-related markers including ALP, Runt-related transcription factor 2 (RUNX2), osteocalcin (OCN), and osteopontin (OPN). The primer sequences were listed in Table S1.

On day 21, alizarin red S (ARS) staining was conducted to visualize calcium nodes. The hPDLSCs were fixed and stained with ARS solution (OriCell, China) for 15 min, followed by three washes with ddH$_2$O. Stained mineral nodules were photographed using a stereomicroscope (Leica, Germany). Subsequently, the stained mineral nodes were desorbed by 10 % (w/v) cetylpyridinium chloride (Aladdin,China) and the absorbance at 562 nm (OD$_{562}$) was measured with a microplate reader (SynergyH1, Bio-Tek, USA) to semi-quantitatively assess the mineral deposition in different groups.

4.19. In vitro immunomodulatory mechanism of J-CeM@Au by transcriptome sequencing

The adhered macrophages in 6-well plates were stimulated with LPS for 12 h as mentioned earlier. Subsequently, the medium was replaced with nomal medium and J-CeM@Au-containing medium. The J-CeM@Au group was irradiated with NIR laser for 5 min as previously described. After 24 h, the macrophages were lysed using RNAiso Plus (Takara Bio, Japan) and stored at −80 °C prior to sequencing. Bulk RNA-seq libraries, raw data collection (FASTQ), alignment (HISAT2), mapping and differential expression analysis (DESeq2) were performed according to the manufacturer's instructions (Novogene, China). The data were normalized using the fragments per kilobase per million reads (FPKM) method. Gene ontology (GO) and KEGG pathway enrichment analyses were performed using the free online NovoMagic Cloud Platform.

4.20. In vitro immunomodulatory mechanism of J-CeM@Au by RT-qPCR and Western blot (WB)

The transcriptome sequencing analysis was further validated by RT-qPCR and WB. The expression levels of IKKα, IKKβ and p65 genes were analyzed by RT-qPCR. The procedures for RT-qPCR were described previously. The primer sequences were listed in Table S1. NF-κB signal pathway proteins (*p*-p65, and p65, *p*-IKKα, IKKα, *p*-IKKβ, IKKβ, *p*-IκBα, IκBα), and glyceraldehyde 3-phosphate dehydrogenase (GAPDH) were detected by WB. Breifly, Proteins were extracted using a RIPA buffer (Aspen, China) on ice, followed by sonication and centrifugation. The proteins were separated using SDS-PAGE and transferred to a PVDF membrane (Millipore, USA). The membrane was blocked with 5 % dehydrated milk in PBS for 1 h, followed by overnight incubation with primary antibodies (*p*-p65, and p65, *p*-IKKα, IKKα, *p*-IKKβ, IKKβ, *p*-IκBα, IκBα, and GAPDH) at 4 °C. After incubation with a secondary antibody (Aspen, China) for 1 h at room temperature, immunoreactive protein bands were visualized using an ECL kit (Aspen, China).

4.21. Anti-planktonic bacterial experiment

Bacterial Culture: *Porphyromonas gingivalis* (*P. g*, ATCC33277) and *Fusobacterium nucleatum* (*F. n*, ATCC25586) were obtained from the Shanghai Bioresource Collection Center. *P. g* was cultured in Tryptic Soy Broth (TSB) as the liquid medium and sheep blood agar medium as the solid medium. Both media were supplemented with yeast extract (5 g/L), L-cysteine (0.5 g/L), vitamin K1 (1 mg/L), and hemin (5 mg/L). *F. n* was cultured in Schaedler Broth as the liquid medium and Columbia blood agar medium as the solid medium. *P. g* and *F. n* were cultured in an anaerobic atmosphere containing 21 % CO_2 and 78.9 % N_2.

The *in vitro* anti-planktonic bacterial efficacy of J-CeM@Au against *P. g* and *F. n* was assessed using the spread plate method and measuring the absorbance of bacterial suspensions at OD_{600}. Briefly, 1 ml of *P. g* ($\sim$10^9 CFU/mL) or *F. n* ($\sim$10^9 CFU/mL) suspension was mixed with 1 mL sterile PBS (as a control), MSN (400 μg/mL), CeO_2 (27 μg/mL), CeM (133 μg/mL), CS-CeM@Au (400 μg/mL), or J-CeM@Au (400 μg/mL) in 5 mL centrifuge tubes. The tubes were then subjected to NIR laser (1W/cm^2) irradiation for 5 min. Subsequently, the 80 μL of serially diluted bacterial solution was spread onto sheep blood agar plates and anaerobically incubated at 37 °C for 7 days. Meanwhile, the remaining suspensions were anaerobically incubated for 12 h and then transferred to a 96-well plate for absorbance measurement at OD_{600} by a microplate reader. Finally, the bacterial colonies were counted, and the bacterial viability was calculated using the following equation:

Bacterial Viability (%) = E/C × 100%,

in which C represents the CFUs in the control group and E represents the CFUs in the experimental groups. Each experiment was repeated 3 times.

Other methods including morphology observation by scanning electron microscope (SEM, CLARA, TESCAN, Czech) and live/dead bacteria staining assay were conducted to assess the anti-planktonic bacterial ability of J-CeM@Au. Results were detailed in SI.

4.22. Biofilm formation

Dual-species biofilms of *P. g* and *F. n* were established as an *in vitro* model to evaluate the anti-biofilm efficacy of J-CeM@Au. Initially, *P. g* (10^7 CFU/mL, 1 mL) was inoculated into confocal dishes and incubated anaerobically at 37 °C for 3 days. Subsequently, the supernatants were then removed, and *F. n* (10^7 CFU/mL, 1 mL) was added to the dishes, followed by anaerobic incubation at 37 °C for an additional 4 days to form dual-species biofilms.

4.23. Penetration of J-CeM@Au into biofilms

The entire dual-species biofilms were dyed with SYTO9 Green Fluorescent Nucleic Acid stain (Thermo Fisher, USA), while the three NPs, CeM, CS-CeM@Au and J-CeM@Au were fluorescently labeled with Cy3 in red. Subsequently, the suspensions of the three NPs were then gently added to the biofilm, and the biofilm was subjected to NIR laser irradiation for 5 min. The morphology of the biofilm and the distribution of NPs before and after NIR laser irradiation were observed and recorded by CLSM (Leica, Germany). The CLSM photos were imported into FIJI software for measuring the penetration depth of Cy3-labeled NPs from the biofilm surface to the depth where the red fluorescence intensity suddenly decreased.

4.24. Antibiofilm activity of J-CeM@Au

Once the biofilms formed in the confocal dishes, the NPs suspensions were gently added to the biofilms, and subsequently subjected to NIR laser irradiation for 5 min. The bactericidal effect of J-Ce@MSN on the biofilms was analyzed using live/dead bacteria staining with a mixture of SYTO9 and PI dyes (Thermo Fisher, USA). Subsequently, the stained biofilms were imaged using CLSM (Leica, Germany).

Dual-species biofilms of *P. g* and *F. n* were formed in the 24-well plates using the same method as previously described. Subsequently, the biofilms were treated with different NPs with NIR irradiation. Next, the treated biofilms in each group were stained with crystalline violet (0.1 %) for 15 min, followed by three rinses with PBS. Finally, the crystalline violet was dissolved in 33 % acetic acid and the absorbance at 600 nm (OD_{600}) of the resulting solution was measured by a microplate reader.

The morphologies of biofilms after different treatments were observed by SEM. The biofilms were formed on sterilized 10 mm glass slides placed in 48-well plates and treated with NPs as described previously. Next, the biofilms were fixed in a glutaraldehyde solution (2.5 wt%) overnight at 4 °C and then dehydrated by ethanol with serial concentration of 30 %, 50 %, 70 %, 90 %, 95 % and 100 %. Finally, the slides with the biofilms were dried in vacuum for SEM scanning.

4.25. Animal model and therapeutic methods

The animal experiments received approval from the Ethics Committee of School of Stomatology, Wuhan University (Project Number: S07922100A). Six-week-old male Sprague-Dawley (SD) rats were obtained from the Hubei Experimental Animal Research Center and randomly assigned to six groups. The rats were housed in the specific-pathogen-free (SPF) conditions and underwent a one-week quarantine period before the experiment. Experimental periodontitis was induced by placing 4-0 silk sutures and injecting suspensions of *P. g* (5 × 10^8 CFU/mL, 100 μL) into the subgingival area around the cervical region of the second molar teeth on both sides of the maxilla in five experimental periodontitis groups for 1 week. A separate group of healthy rats served as the control group. Subsequently, the ligation sites of rats with periodontitis were subjected to different treatments (P + Saline, P + Saline + NIR, P + CeM + NIR, P + CS-CeM@Au + NIR and P + J-CeM@Au + NIR) every 3 days for five consecutive treatments. The control group received no treatment and was fed normally. Finally, the rats were euthanized, and the maxillae and gingival tissues were surgically excised for further analysis. All procedures performed on rats were carried out under anesthesia by the same operators.

4.26. In vivo antibacterial effect assessment

For *in vivo* antibacterial effect evaluation, the gingival cervical fluid of the treated gingival sulcus was assessed by standard plate counting at the end of the treatment. Briefly, sterile swabs were used to probe treatment site and were then immediately immersed in 1 mL of sterile PBS solution. Then, bacterial colonies were quantified using the dilution plate method (diluted by 10^5 times) after incubation for 72 h at 37 °C anaerobically.

4.27. In vivo assessment of ROS scavenging

At the end of treatment with NP suspensions, DCFH-DA, a fluorescence probe, was enjected *in situ* into the periodontal pockets for ROS detection. After a 10-min incubation period, the fluorescence imaging was performed using a small animal imaging system (PerkinElmer, IVIS Spectrum, USA).

4.28. In vivo flow cytometry analysis of macrophage polarization

Lingual and buccal gingival tissues around the ligated molars of every rat were collected (n = 3 per group) and digested with collagenase type II (2 mg/ml, Biosharp) and collagenase type IV (2 mg/ml, Biosharp) for 2 h at 37 °C. The suspensions were then filtered with a 70 μm cell-strainer to remove tissue fragments. For surface antigen staining, CD11b/c-PE/Cyanine7 (1:200, BioLegend) and CD68-FITC (1:200, BioLegend) antibodies were used as pan-macrophage makers, and CD86-
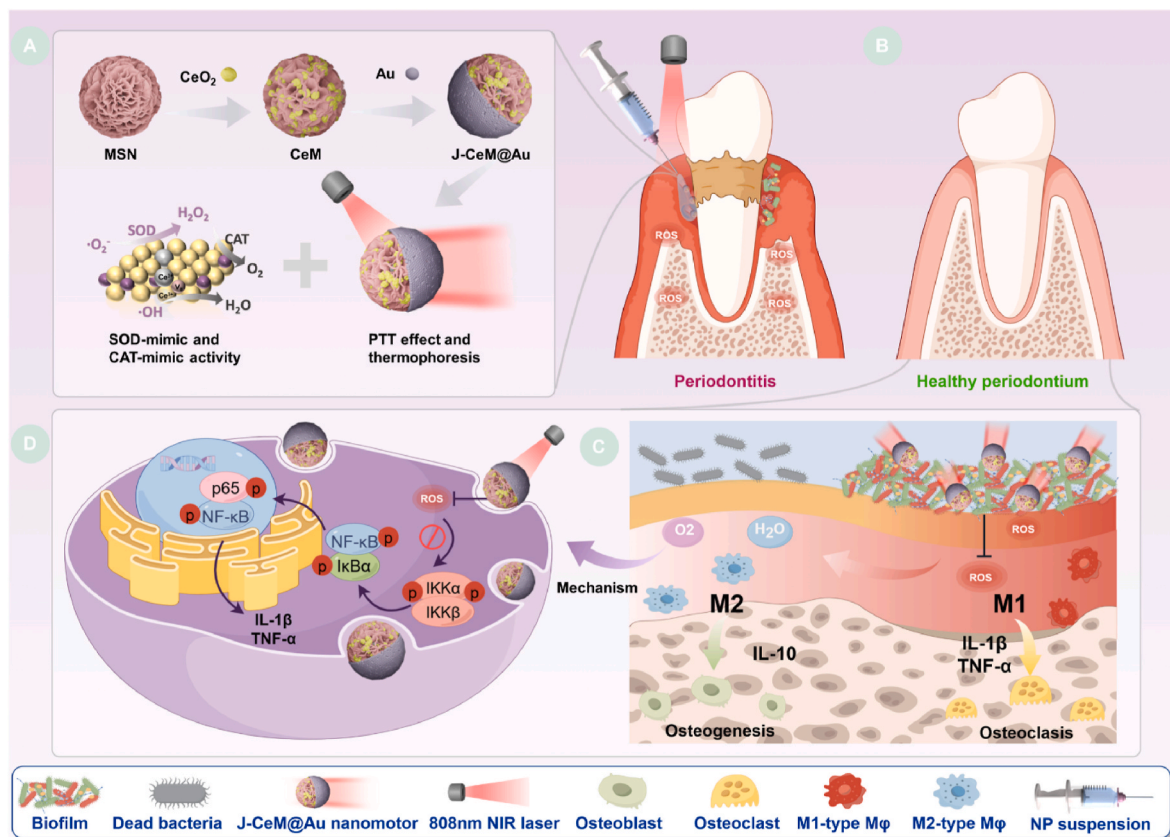
Scheme 1. The synthesis process and therapeutic mechanism of J-CeM@Au. (A). Illustration for the preparation process of J-CeM@Au. (B ~ C) Illumination of the multifunctional J-CeM@Au for accelerating periodontitis healing by biofilm eradicating and ROS scavenging. (D) Mechanisms for the immunomodulation of J-CeM@Au.

APC (1:200, BioLegend) antibody was used to detect M1 macrophages. For transmembrane antigen staining, the cell suspensions were fixed and permeabilized, and then stained with CD206-PE (1:200, BioLegend) to detect M2 macrophages. Flow cytometry of the stained cells was performed using an Cytoflex flow cytometer (Beckman, USA) and analyzed by Flowjo.

4.29. Micro-CT analysis of periodontal bone loss

Following fixation in 4 % paraformaldehyde for 48 h, all harvested maxillary tissues were scanned by a Micro-CT scanner (Skyscan 1276, Bruker, Germany). The samples underwent three-dimensional reconstruction and two-dimensional imaging using CTvox and DataViewer software. Scanned data were analyzed by CT Analyser software.

4.30. Histological assessment

The maxillary samples, which had already been already treated by 4 % formaldehyde, were transferred to ethylene diamine tetraacetic acid (EDTA) solution for decalcification. After a month, the decalcified samples were dehydrated in a gradient alcohol and embedded in paraffin to prepare tissue slices. H&E and Masson's trichrome staining were conducted to assess periodontal inflammation and tissue repair. Additionally, IF and IHC staining were performed to analyze the levels of inflammation in the periodontal tissues.

4.31. In vivo biosafety evaluation

Hematology tests were performed to assess potential cytotoxicity and levels of inflammation. Bood cell counts, including WBC, RBC, Lymph, Mid, Gran; plasma proteins, including TP, ALB and GLO; liver function

markers, including ALT, AST, TBIL; and renal function markrs, including CRE and urea, were tested from whole blood of the experimental rats. In addition, vital organs such as the heart, liver, spleen, lung, and kidney were subjected to HE staining.

4.32. Statistical analysis

Statistical analysis was performed using GraphPad Prism version 9.5.1 (GraphPad Software Inc., CA, USA). Multiple groups were compared using a one-way analysis of variance (ANOVA) test with Tukey's multiple comparisons test. The symbols used in the statistical analysis were as follows: "n.s." represented "not significant", "*" represented "$p < 0.05$", "**" represented "$p < 0.01$", "***" represented "$p < 0.001$", and "****" represented "$p < 0.0001$". The data were presented as mean ± standard deviation (SD) when n ≥ 3.

Ethics approval and consent to participate

Experimental procedures were approved by the Ethics Committee of School of Stomatology, Wuhan University (Project Number: S07922100A).

CRediT authorship contribution statement

Xuan Bai: Writing – original draft, Software, Methodology, Formal analysis, Conceptualization. **Wenan Peng:** Writing – review & editing, Software, Methodology, Formal analysis, Data curation. **Ying Tang:** Methodology. **Ziming Wang:** Methodology. **Jingmei Guo:** Methodology. **Fangfang Song:** Methodology. **Hongye Yang:** Methodology. **Cui Huang:** Writing – review & editing, Project administration, Funding acquisition, Conceptualization.

Declaration of competing interest

The authors declare that they have no known competing financial interests or personal relationships that could have appeared to influence the work reported in this paper.

Appendix A. Supplementary data

Supplementary data to this article can be found online at https://doi.org/10.1016/j.bioactmat.2024.07.014.

Appendix A. Supplementary data

Supplementary data to this article can be found online.

References

[1] M.A. Peres, L.M.D. Macpherson, R.J. Weyant, B. Daly, R. Venturelli, M.R. Mathur, S. Listl, R.K. Celeste, C.C. Guarnizo-Herreño, C. Kearns, H. Benzian, P. Allison, R.G. Watt, Oral diseases: a global public health challenge, Lancet 394 (10194) (2019) 249–260.

[2] G. Hajishengallis, T. Chavakis, Local and systemic mechanisms linking periodontal disease and inflammatory comorbidities, Nat. Rev. Immunol. 21 (7) (2021) 426–440.

[3] M.G. Balta, E. Papathanasiou, I.J. Blix, T.E. Van Dyke, Host modulation and treatment of periodontal disease, J. Dent. Res. 100 (8) (2021) 798–809.

[4] S. Ji, Y. Choi, Microbial and host factors that affect bacterial invasion of the gingiva, J. Dent. Res. 99 (9) (2020) 1013–1020.

[5] G. Gabarrini, S. Grasso, A.J.v. Winkelhoff, J.M.v. Dijl, Gingimaps: protein localization in the oral pathogen *Porphyromonas gingivalis*, Microbiol. Mol. Biol. Rev. 84 (1) (2020) e00032.

[6] K. Pandi, S. Angabo, J. Gnanasekaran, H. Makkawi, L. Eli-Berchoer, F. Glaser, G. Nussbaum, Porphyromonas gingivalis induction of TLR2 association with Vinculin enables PI3K activation and immune evasion, PLoS Pathog. 19 (4) (2023) e1011284.

[7] J.-y. Gu, Y.-j. Liu, X.-q. Zhu, J.-y. Qiu, Y. Sun, Effects of endotoxin tolerance induced by Porphyromonas gingivalis lipopolysaccharide on inflammatory responses in neutrophils, Inflammation 43 (5) (2020) 1692–1706.

[8] C.A. Brennan, W.S. Garrett, Fusobacterium nucleatum —symbiont, opportunist and oncobacterium, Nat. Rev. Microbiol. 17 (3) (2019) 156–166.

[9] T. Lazarov, S. Juarez-Carreño, N. Cox, F. Geissmann, Physiology and diseases of tissue-resident macrophages, Nature 618 (7966) (2023) 698–707.

[10] M. Locati, G. Curtale, A. Mantovani, Diversity, mechanisms, and significance of macrophage plasticity, Annu. Rev. Pathol. 15 (2020) 123–147.

[11] J.D. Hathaway-Schrader, C.M. Novince, Maintaining homeostatic control of periodontal bone tissue, Periodontol 86 (1) (2021) 157–187, 2000.

[12] O.R. Mahon, D.C. Browe, T. Gonzalez-Fernandez, P. Pitacco, I.T. Whelan, S. Von Euw, C. Hobbs, V. Nicolosi, K.T. Cunningham, K.H.G. Mills, D.J. Kelly, A. Dunne, Nano-particle mediated M2 macrophage polarization enhances bone formation and MSC osteogenesis in an IL-10 dependent manner, Biomaterials 239 (2020) 119833.

[13] F.V. Ribeiro, J.J. Mehta, M.F. Monteiro, J. Moore, M.Z. Casati, L. Nibali, Minimal invasiveness in nonsurgical periodontal therapy, Periodontol 91 (1) (2023) 7–19, 2000.

[14] D. Herrera, A.J. van Winkelhoff, P. Matesanz, K. Lauwens, W. Teughels, Europe's contribution to the evaluation of the use of systemic antimicrobials in the treatment of periodontitis, Periodontol (2023) 1–28, 2000 00.

[15] K. Jepsen, A. Sculean, S. Jepsen, Complications and treatment errors related to regenerative periodontal surgery, Periodontol 92 (1) (2023) 120–134, 2000.

[16] K. Jepsen, W. Falk, F. Brune, R. Fimmers, S. Jepsen, I. Bekeredjian-Ding, Prevalence and antibiotic susceptibility trends of periodontal pathogens in the subgingival microbiota of German periodontitis patients: a retrospective surveillance study, J. Clin. Periodontol. 48 (9) (2021) 1216–1227.

[17] P. Makvandi, H. Song, C.K.Y. Yiu, R. Sartorius, E.N. Zare, N. Rabiee, W.-X. Wu, A.C. Paiva-Santos, X.-D. Wang, C.-Z. Yu, F.R. Tay, Bioengineered materials with selective antimicrobial toxicity in biomedicine, Mil. Med. Res. 10 (1) (2023) 8.

[18] J. Liu, Y. Wang, Q. Shi, X. Wang, P. Zou, M. Zheng, Q. Luan, Mitochondrial DNA efflux maintained in gingival fibroblasts of patients with periodontitis through ROS/mPTP pathway, Oxid. Med. Cell. Longev. 2022 (1) (2022) 1000213.

[19] F.S.C. Sczepanik, M.L. Grossi, M. Casati, M. Goldberg, M. Glogauer, N. Fine, H.C. Tenenbaum, Periodontitis is an inflammatory disease of oxidative stress: we should treat it that way, Periodontol 84 (1) (2020) 45–68, 2000.

[20] C. Damgaard, A. Kantarci, P. Holmstrup, H. Hasturk, C.H. Nielsen, T.E. Van Dyke, Porphyromonas gingivalis-induced production of reactive oxygen species, tumor necrosis factor-α, interleukin-6, CXCL8 and CCL2 by neutrophils from localized aggressive periodontitis and healthy donors: modulating actions of red blood cells and resolvin E1, J. Periodontal. Res. 52 (2) (2017) 246–254.

[21] B. Zhang, Y. Yang, J. Yi, Z. Zhao, R. Ye, Hyperglycemia modulates M1/M2 macrophage polarization via reactive oxygen species overproduction in ligature-induced periodontitis, J. Periodontal. Res. 56 (5) (2021) 991–1005.

[22] Y. Yu, S. Zhao, D. Gu, B. Zhu, H. Liu, W. Wu, J. Wu, H. Wei, L. Miao, Cerium oxide nanozyme attenuates periodontal bone destruction by inhibiting the ROS–NFκB pathway, Nanoscale 14 (7) (2022) 2628–2637.

[23] Y. Weng, H. Wang, L. Li, Y. Feng, S. Xu, Z. Wang, Trem2 mediated Syk-dependent ROS amplification is essential for osteoclastogenesis in periodontitis microenvironment, Redox Biol. 40 (2021) 101849.

[24] J. Guo, Z. Xing, L. Liu, Y. Sun, H. Zhou, M. Bai, X. Liu, M. Adeli, C. Cheng, X. Han, Antioxidase-like nanobiocatalysts with ultrafast and reversible redox-centers to secure stem cells and periodontal tissues, Adv. Funct. Mater. 33 (15) (2023) 2211778.

[25] Y. Xie, S. Xiao, L. Huang, J. Guo, M. Bai, Y. Gao, H. Zhou, L. Qiu, C. Cheng, X. Han, Cascade and ultrafast artificial antioxidases alleviate inflammation and bone resorption in periodontitis, ACS Nano 17 (15) (2023) 15097–15112.

[26] Y. Zhang, S. Zhao, J. Feng, S. Song, W. Shi, D. Wang, H. Zhang, Unraveling the physical chemistry and materials science of CeO$_2$-based nanostructures, Chem 7 (8) (2021) 2022–2059.

[27] M.H. Golnaz Heidari, Fereshteh Nejaddehbashi, Mohammad Reza Sarfjoo, Satar Yousefiasl, Esmaeel Sharifi, Ashkan Bigham, Tarun Agarwal, Assunta Borzacchiello, Elena Lagreca, Concetta Di Natale, Nasser Nikfarjam, Yasser Vasseghian, Biosynthesized nanomaterials with antioxidant and antimicrobial properties, mater, Chem. Horizons 1 (1) (2022) 35–48.

[28] M. Ziemba, C. Schilling, M.V. Ganduglia-Pirovano, C. Hess, Toward an atomic-level understanding of ceria-based catalysts: when experiment and theory go hand in hand, Acc. Chem. Res. 54 (13) (2021) 2884–2893.

[29] I. Pezzini, A. Marino, S. Del Turco, C. Nesti, S. Doccini, V. Cappello, M. Gemmi, P. Parlanti, F.M. Santorelli, V. Mattoli, G. Ciofani, Cerium oxide nanoparticles: the regenerative redox machine in bioenergetic imbalance, Nanomedicine 12 (4) (2017) 403–416.

[30] C. Liu, L. Gui, J.-J. Zheng, Y.-Q. Xu, B. Song, L. Yi, Y. Jia, A. Taledaohan, Y. Wang, X. Gao, Z.-Y. Qiao, H. Wang, Z. Tang, Intrinsic strain-mediated ultrathin ceria nanoantioxidant, J. Am. Chem. Soc. 145 (34) (2023) 19086–19097.

[31] Y.G. Kim, Y. Lee, N. Lee, M. Soh, D. Kim, T. Hyeon, Ceria-based therapeutic antioxidants for biomedical applications, Adv. Mater. 36 (10) (2024) 2210819.

[32] S. Zhou, H. Cai, X. He, Z. Tang, S. Lu, Enzyme-mimetic antioxidant nanomaterials for ROS scavenging: design, classification, and biological applications, Coord. Chem. Rev. 500 (2024) 215536.

[33] J. Huo, Q. Jia, H. Huang, J. Zhang, P. Li, X. Dong, W. Huang, Emerging photothermal-derived multimodal synergistic therapy in combating bacterial infections, Chem. Soc. Rev. 50 (15) (2021) 8762–8789.

[34] H. Yuan, Z. Li, Q. Zhao, S. Jia, T. Wang, L. Xu, H. Yuan, S. Li, Molecular evolution of acceptor–donor–acceptor-type conjugated oligomer nanoparticles for efficient photothermal antimicrobial therapy, Adv. Funct. Mater. 33 (21) (2023) 2213209.

[35] J. Zheng, X. Cheng, H. Zhang, X. Bai, R. Ai, L. Shao, J. Wang, Gold nanorods: the most versatile plasmonic nanoparticles, Chem. Rev. 121 (21) (2021) 13342–13453.

[36] G.X. Minmin Shao, Guiqing He, bacterial synthesis of metallic nanoparticles for biomedical applications, Mater. Chem. Horizons 2 (4) (2023) 303–313.

[37] S. Yougbaré, H.-L. Chou, C.-H. Yang, D.I. Krisnawati, A. Jazidie, M. Nuh, T.-R. Kuo, Facet-dependent gold nanocrystals for effective photothermal killing of bacteria, J. Hazard Mater. 407 (2021) 124617.

[38] N. Yang, Y. Kang, Y. Cong, X. Wang, C. Yao, S. Wang, L. Li, Controllable gold nanocluster–emulsion interface for direct cell penetration and photothermal killing, Adv. Mater. 35 (50) (2023) 2208349.

[39] R.-L. Ge, P.-N. Yan, Y. Liu, Z.-S. Li, S.-Q. Shen, Y. Yu, Recent advances and clinical potential of near infrared photothermal conversion materials for photothermal hepatocellular carcinoma therapy, Adv. Funct. Mater. 33 (29) (2023) 2301138.

[40] M.J. Mitchell, M.M. Billingsley, R.M. Haley, M.E. Wechsler, N.A. Peppas, R. Langer, Engineering precision nanoparticles for drug delivery, Nat. Rev. Drug Discov. 20 (2) (2021) 101–124.

[41] W. Najahi-Missaoui, R.D. Arnold, B.S. Cummings, Safe nanoparticles: are we there yet? Int. J. Mol. Sci. 22 (1) (2021) 385.

[42] C. Gao, Y. Wang, Z. Ye, Z. Lin, X. Ma, Q. He, Biomedical micro-/nanomotors: from overcoming biological barriers to in vivo imaging, Adv. Mater. 33 (6) (2021) 2000512.

[43] T. Maric, A. Løvind, Z. Zhang, J. Geng, A. Boisen, Near-infrared light-driven mesoporous SiO2/Au nanomotors for eradication of Pseudomonas aeruginosa biofilm, Adv. Healthcare Mater. 12 (13) (2023) 2203018.

[44] S. Zhang, J. Chen, M.-L. Lian, W.-S. Yang, X. Chen, An engineered, self-propelled nanozyme as reactive oxygen species scavenger, Chem. Eng. J. (Amsterdam, Neth.) 446 (2022) 136794.

[45] S. Gao, H. Jia, H. Zhang, H. Yao, Y. Chen, J. Shi, Nanocatalytic tumor therapy by biomimetic dual inorganic nanozyme-catalyzed cascade reaction, Adv. Sci. 6 (3) (2019) 1801733.

[46] H. Wu, F. Li, S. Wang, J. Lu, J. Li, Y. Du, X. Sun, X. Chen, J. Gao, D. Ling, Ceria nanocrystals decorated mesoporous silica nanoparticle based ROS-scavenging

tissue adhesive for highly efficient regenerative wound healing, Biomaterials 151 (2018) 66–77.

[47] M. Liu, L. Chen, Z. Zhao, M. Liu, T. Zhao, Y. Ma, Q. Zhou, Y.S. Ibrahim, A. A. Elzatahry, X. Li, D. Zhao, Enzyme-based mesoporous nanomotors with near-infrared optical brakes, J. Am. Chem. Soc. 144 (9) (2022) 3892–3901.

[48] Y. Ma, Z. Tian, W. Zhai, Y. Qu, Insights on catalytic mechanism of CeO$_2$ as multiple nanozymes, Nano Res. 15 (12) (2022) 10328–10342.

[49] S. Ren, Y. Zhou, R. Fan, W. Peng, X. Xu, L. Li, Y. Xu, Constructing biocompatible MSN@Ce@PEG nanoplatform for enhancing regenerative capability of stem cell via ROS-scavenging in periodontitis, Chem. Eng. J. (Amsterdam, Neth.) 423 (2021) 130207.

[50] C. Xu, Y. Jiang, H. Wang, Y. Zhang, Y. Ye, H. Qin, J. Gao, Q. Dan, L. Du, L. Liu, F. Peng, Y. Li, Y. Tu, Arthritic microenvironment actuated nanomotors for active rheumatoid arthritis therapy, Adv. Sci. 10 (4) (2023) 2204881.

[51] C. Chen, G. Chu, W. He, Y. Liu, K. Dai, J. Valdez, A. Moores, P. Huang, Z. Wang, J. Jin, M. Guan, W. Jiang, Y. Mai, D. Ma, Y. Wang, Y. Zhou, A Janus Au–polymersome heterostructure with near-field enhancement effect for implant-associated infection phototherapy, Adv. Mater. 35 (3) (2023) 2207950.

[52] T. Liu, C. Guo, W. Li, S. Fan, Thermal photonics with broken symmetries, eLight 2 (1) (2022) 25.

[53] H. Šípová-Jungová, D. Andrén, S. Jones, M. Käll, Nanoscale inorganic motors driven by light: principles, realizations, and opportunities, Chem. Rev. 120 (1) (2020) 269–287.

[54] A. Olona, C. Hateley, S. Muralidharan, M.R. Wenk, F. Torta, J. Behmoaras, Sphingolipid metabolism during Toll-like receptor 4 (TLR4)-mediated macrophage activation, Br. J. Pharmacol. 178 (23) (2021) 4575–4587.

[55] P. Ming, Y. Liu, P. Yu, X. Jiang, L. Yuan, S. Cai, P. Rao, R. Cai, X. Lan, G. Tao, J. Xiao, A biomimetic Se-nHA/PC composite microsphere with synergistic immunomodulatory and osteogenic ability to activate bone regeneration in periodontitis, Small 20 (9) (2024) 2305490.

[56] J. Gong, C. Ye, J. Ran, X. Xiong, X. Fang, X. Zhou, Y. Yi, X. Lu, J. Wang, C. Xie, J. Liu, Polydopamine-mediated immunomodulatory patch for diabetic periodontal tissue regeneration assisted by metformin-ZIF system, ACS Nano 17 (17) (2023) 16573–16586.

[57] X.-T. He, X. Li, Y. Yin, R.-X. Wu, X.-Y. Xu, F.-M. Chen, The effects of conditioned media generated by polarized macrophages on the cellular behaviours of bone marrow mesenchymal stem cells, J. Cell Mol. Med. 22 (2) (2018) 1302–1315.

[58] B. Depalle, C.M. McGilvery, S. Nobakhti, N. Aldegaither, S.J. Shefelbine, A. E. Porter, Osteopontin regulates type I collagen fibril formation in bone tissue, Acta Biomater. 120 (2021) 194–202.

[59] M. Chen, Y. Zhang, P. Zhou, X. Liu, H. Zhao, X. Zhou, Q. Gu, B. Li, X. Zhu, Q. Shi, Substrate stiffness modulates bone marrow-derived macrophage polarization through NF-κB signaling pathway, Bioact. Mater. 5 (4) (2020) 880–890.

[60] H. Sun, Z. Sun, X. Xu, Z. Lv, J. Li, R. Wu, Y. Fei, G. Tan, Z. Liu, Y. Liu, D. Shi, Blocking TRPV4 ameliorates osteoarthritis by inhibiting M1 macrophage polarization via the ROS/NLRP3 signaling pathway, Antioxidants 11 (12) (2022) 2315.

[61] L. Abusleme, A. Hoare, B.-Y. Hong, P.I. Diaz, Microbial signatures of health, gingivitis, and periodontitis, Periodontol 86 (1) (2021) 57–78, 2000.

[62] Q. Kong, M. Qi, W. Li, Y. Shi, J. Su, S. Xiao, J. Sun, X. Bai, B. Dong, L. Wang, A novel Z-scheme heterostructured Bi2S3/Cu-tcpp nanocomposite with

[63] Z. Yin, Y. Liu, A. Anniwaer, Y. You, J. Guo, Y. Tang, L. Fu, L. Yi, C. Huang, Rational designs of biomaterials for combating oral biofilm infections, Adv. Mater. (2023) 2305633.

[64] X. Lv, L. Wang, A. Mei, Y. Xu, X. Ruan, W. Wang, J. Shao, D. Yang, X. Dong, Recent nanotechnologies to overcome the bacterial biofilm matrix barriers, Small 19 (6) (2023) 2206220.

[65] C.R. Arciola, D. Campoccia, L. Montanaro, Implant infections: adhesion, biofilm formation and immune evasion, Nat. Rev. Microbiol. 16 (7) (2018) 397–409.

[66] J.L. Baker, J.L. Mark Welch, K.M. Kauffman, J.S. McLean, X. He, The oral microbiome: diversity, biogeography and human health, Nat. Rev. Microbiol. 22 (2) (2024) 89–104.

[67] Y. Hu, H. Li, X. Lv, Y. Xu, Y. Xie, L. Yuwen, Y. Song, S. Li, J. Shao, D. Yang, Stimuli-responsive therapeutic systems for the treatment of diabetic infected wounds, Nanoscale 14 (36) (2022) 12967–12983.

[68] X. Sun, M. Wei, X. Pang, L. Lin, Q. Gao, L. Su, T. Liu, Y. Yao, J. Song, W. Wang, X. Yan, Sonodynamic bacterial inactivation enhanced by an actuator-integrated mechanism, Adv. Funct. Mater. 33 (30) (2023) 2214619.

[69] N.S. Jakubovics, S.D. Goodman, L. Mashburn-Warren, G.P. Stafford, F. Cieplik, The dental plaque biofilm matrix, Periodontol 86 (1) (2021) 32–56, 2000.

[70] M.C. Sánchez, A. Alonso-Español, H. Ribeiro-Vidal, B. Alonso, D. Herrera, M. Sanz, Relevance of biofilm models in periodontal Research: from static to dynamic systems, Microorganisms 9 (2) (2021) 428.

[71] B. Yu, C.-Y. Wang, Osteoporosis and periodontal diseases – an update on their association and mechanistic links, Periodontol 89 (1) (2022) 99–113, 2000.

[72] K. Chen, Y. Liu, J. He, N. Pavlos, C. Wang, J. Kenny, J. Yuan, Q. Zhang, J. Xu, W. He, Steroid-induced osteonecrosis of the femoral head reveals enhanced reactive oxygen species and hyperactive osteoclasts, Int. J. Biol. Sci. 16 (11) (2020) 1888–1900.

[73] M.P. Murphy, H. Bayir, V. Belousov, C.J. Chang, K.J.A. Davies, M.J. Davies, T. P. Dick, T. Finkel, H.J. Forman, Y. Janssen-Heininger, D. Gems, V.E. Kagan, B. Kalyanaraman, N.-G. Larsson, G.L. Milne, T. Nyström, H.E. Poulsen, R. Radi, H. Van Remmen, P.T. Schumacker, P.J. Thornalley, S. Toyokuni, C.C. Winterbourn, H. Yin, B. Halliwell, Guidelines for measuring reactive oxygen species and oxidative damage in cells and in vivo, Nat. Metab. 4 (6) (2022) 651–662.

[74] H. Ping, W. Wagermaier, N. Horbelt, E. Scoppola, C. Li, P. Werner, Z. Fu, P. Fratzl, Mineralization generates megapascal contractile stresses in collagen fibrils, Science 376 (6589) (2022) 188–192.

[75] S. Dong, Y. Dong, T. Jia, S. Liu, J. Liu, D. Yang, F. He, S. Gai, P. Yang, J. Lin, GSH-depleted nanozymes with hyperthermia-enhanced dual enzyme-mimic activities for tumor nanocatalytic therapy, Adv. Mater. 32 (42) (2020) 2002439.

[76] T. Maric, M.Z.M. Nasir, R.D. Webster, M. Pumera, Tailoring metal/TiO2 interface to influence motion of light-activated Janus micromotors, Adv. Funct. Mater. 30 (9) (2020) 1908614.

[77] B. Seong, S. Bock, E. Hahm, K.-H. Huynh, J. Kim, S.H. Lee, X.-H. Pham, B.-H. Jun, Synthesis of densely immobilized gold-assembled silica nanostructures, Int. J. Mol. Sci. 22 (5) (2021) 2543.

[78] J. Liu, X. Wang, M. Zheng, Q. Luan, Oxidative stress in human gingival fibroblasts from periodontitis versus healthy counterparts, Oral Dis. 29 (3) (2023) 1214–1225.